

Boundary-layer modeling of polymer-based acoustofluidic devices

Sazid Z. Hoque* and Henrik Bruus†

*Department of Physics, Technical University of Denmark,
DTU Physics Building 309, DK-2800 Kongens Lyngby, Denmark*

(Dated: 7 July 2025, DRAFT)

In fluid-filled microchannels embedded in solid devices and driven by MHz ultrasound transducers, the thickness of the viscous boundary layer in the fluid near the confining walls is typically 3 to 4 orders of magnitude smaller than the acoustic wavelength and 5 orders of magnitude smaller than the longest dimension of the device. This large span in length scale renders direct numerical simulations of such devices prohibitively expensive in terms of computer memory requirements, and consequently, the so-called boundary-layer models are introduced. In such models, approximate analytical expressions of the boundary-layer fields are found and inserted in the governing equations and boundary conditions for the remaining bulk fields. Since the bulk fields do not vary across the boundary layers, they can be computed numerically using the resulting boundary-layer model without resolving the boundary layers. However, current boundary-layer models are only accurate for hard solids (*e.g.* glass and silicon) with relatively small oscillation amplitudes of the confining wall, and they fail for soft solids (*e.g.* polymers) with larger wall oscillations. In this work, we extend the boundary-layer model of Bach and Bruus, *J. Acoust. Soc. Am.* **144**, 766 (2018) to enable accurate simulation of soft-walled devices. The extended model is validated by comparing (1) with direct numerical simulations in three and two dimensions of tiny sub-mm and larger mm-sized polymer devices, respectively, and (2) with previously published experimental data.

I. INTRODUCTION

Acoustofluidic devices based on bulk acoustic waves show promising applications in contactless manipulation of micro-objects [1, 2] such as separation of bacteria from blood lysate [3], cancer cells enrichment in blood [4, 5], optimized microparticle focusing [6, 7], and other cell manipulations [8]. These devices are also used for manipulation of immiscible fluid interfaces [9, 10] and inhomogeneous fluids [11–14].

Traditionally, bulk-acoustic-wave devices are fabricated using hard materials with high Q factors, such as glass and silicon [15]. Although such devices can be manufactured with high accuracy and throughput, the fabrication process may be expensive, limiting in particular their single-use applications. Alternatively, polymer-based devices can be used, which is advantageous for bulk production at minimal cost compared to glass-silicon devices [16–20]. However, it is difficult to establish the acoustic fields in a polymer system due to the low acoustic contrast between the polymer and the fluid. Recently, the formation of pressure nodal planes in polymer systems has been elucidated by Moiseyenko and Bruus [21] by introducing the principle of whole-system ultrasound resonances (WSUR). According to this principle, acoustic resonances in polymer devices are determined by the dimensions of the whole system, and by the acoustic contrast between the ambient air and the system. Among the obtained WSUR modes, the ones leading to a robust acoustic response inside the fluid cavity are selected. Successful focusing of particles in polymer-based acoustoflu-

idic devices designed using the WSUR principle has been demonstrated by experiments and simulations [20].

Despite the significant advancement in numerical modeling of acoustofluidic devices in the last decade [22–26], it remains a challenge to have a robust, computationally efficient method that captures all the relevant length scales of the problem ranging from the length of the device (~ 5 cm) down to the thickness of the viscous boundary layers (~ 0.5 μm) in the fluid, the latter being responsible for the formation of the steady acoustic streaming. Whereas the pressure acoustics, and thus the acoustic radiation force that dominates the dynamics of large particles ($\gtrsim 2$ μm) suspended in the fluid, depends on the acoustic wavelength (~ 500 μm) and not on the acoustic streaming, the dynamics of sub- μm particles are dominated by the viscous Stokes drag from the acoustic streaming. The inclusion of the boundary layers in numerical simulations is therefore crucial for a full understanding of acoustofluidic devices and their applications for sub- μm -particle manipulation in lab-on-a-chip technology [27–30]. Performing direct numerical simulations to capture the entire length-scale range is computationally expensive and poses severe challenges, especially for three-dimensional (3D) simulations.

The effective boundary-layer model introduced by Bach and Bruus in 2018 [31] marked a significant progress towards robust modeling of the thin boundary layer. Based on previous work by Nyborg [32], Lee and Wang [33], and Vanneste and Bühler [34], Bach and Bruus derived approximate analytical expressions for the viscous boundary-layer fields that decays exponentially away from the fluid-solid interface inside the thin boundary layer. Inserting these analytic expressions in the governing equations and boundary conditions, an effective model for the remaining bulk acoustic fields were ob-

* shoque@dtu.dk

† bruus@fysik.dtu.dk

tained. As these bulk fields do not vary on the small boundary-layer length scale, they can be computed numerically without resolving the boundary layer.

The effective boundary-layer model is based on the assumptions that the boundary-layer thickness δ is much smaller than both the radius of curvature of the fluid-solid interface (the wall) and the acoustic wavelength, and that the amplitude of the wall motion in the perpendicular direction is much smaller than δ . 3D versions of the model have been validated against experimental results in two cases. First, Skov *et al.* [35] used the model to simulate a hard-walled glass-silicon device and successfully compared their results with previous experimental work [36], both regarding the 1st-order acoustic fields and the 2nd-order streaming field, although the latter is sensitive to the exact value of the resonance frequency and of detailed shape of the fluid-solid interface. Second, Lickert *et al.* [20] compared simulation results of the model for a soft-walled polymer-based device, and found fairly good agreement with their own experiments regarding the 1st-order acoustic fields, but no studies of the streaming field was performed.

The main goal of this work is to evaluate the 2nd-order time-averaged streaming field using the boundary-layer model for a soft-walled polymer device. We have found that the second assumption above concerning the smallness of the wall oscillation amplitude compared to δ fails in this case, and therefore an extension of the boundary-layer model is needed to accurately determining the acoustic streaming field for soft-walled devices. In this work, we extend the boundary-layer model from 2018 by Bach and Bruus [31], henceforth called the “BL18 model”, by allowing for larger perpendicular wall motions. Introduced in 2025, we call this extended boundary-layer model the “BL25 model”.

The first half of the paper, Secs. II-IV, concerns the development of the theory behind the BL25 model. The basic acoustofluidic perturbation approach as well as the detailed 1st-order expressions for the acoustic fields carry over unchanged (with one minor addition in a boundary condition) from the BL18 model to the BL25 model, which is summarized in Secs. II and III. In Sec. IV, we present the model of the extended 2nd-order streaming field, where we modify the effective slip-boundary condition by (1) taking into account the hitherto neglected short-range 2nd-order pressure field, and (2) including previously omitted higher-order terms in the small parameter $\epsilon = k_0\delta \simeq 0.003$, k_0 being the acoustic wavenumber. The second half of the paper, Secs. V-VIII, concerns the validation of the BL25 model. In Secs. V and VI, respectively, we define the acoustofluidic model devices used for numerical validation of the BL25 model, and we present the implementation of the model for these devices in the finite-element software COMSOL Multiphysics. In Sec. VII, we carry out a numerical validations including a mesh-convergence study of the BL25 model in both two-dimensional (2D) and 3D simulations by comparing it to a “Full model” consisting of direct numerical sim-

ulation of the full perturbation equations using a mesh that resolves the thin boundary layers. The 3D simulation of the Full model is made possible by studying a down-scaled device with a linear size less than 500 μm , which is driven by a thin-film piezoelectric transducer of thickness 2 μm . In Sec. VIII, we validate the BL25 model experimentally by using it to model the polymer-device studied by Lickert *et al.* [20] and comparing the simulation results with the published experimental data. Finally, we end with a summary and concluding remarks in Sec. IX. Some mathematical details are presented in Appendices B, A, C, and D, and supplementing numerical simulations are provided in the Supplemental Material [37], which includes Refs. [20, 38].

II. PERTURBATION EXPANSION OF THE GOVERNING EQUATIONS

In this work, we follow Bach and Bruus [31] closely, and present here a just summary of the BL18 model, while referring the reader to the original paper for details. We consider a system consisting of a fluid domain Ω^{fl} embedded in an elastic solid domain Ω^{sl} , which is actuated by a piezoelectric transducer domain Ω^{pz} attached to a part $\partial\Omega_{\text{pz}}^{\text{sl}}$ of the outer solid surface $\partial\Omega^{\text{sl}}$ and driven by an applied time-harmonic AC voltage $\varphi_0(t) = \varphi_0 e^{-i\omega t}$ with a real-valued amplitude φ_0 at the angular frequency $\omega = 2\pi f$, where f is the frequency in the MHz range. The fluid is described by three basic Eulerian fields, the density ρ , the pressure p , and the velocity \mathbf{v} , and the solid by the basic Lagrangian field, the displacement \mathbf{u} . We assume adiabatic acoustics without thermal transport, so the temperature field is not independent, but follows from the pressure and density. Assuming a sufficiently low actuation amplitude φ_0 , the whole system can be analyzed using a complex-valued perturbation expansion, where any field g depending on position \mathbf{r} and time t has a uniform constant 0th-order component g_0 , a time-harmonic 1st-order component g_1 , and a steady time-averaged 2nd-order component g_2 , proportional to $(\varphi_0)^0$, $(\varphi_0)^1$, and $(\varphi_0)^2$, respectively,

$$g(\mathbf{r}, t) = g_0 + g_1(\mathbf{r}) e^{-i\omega t} + g_2(\mathbf{r}), \quad (1a)$$

$$g^{\text{phys}}(\mathbf{r}, t) = g_0 + \text{Re}[g_1(\mathbf{r}) e^{-i\omega t}] + g_2(\mathbf{r}). \quad (1b)$$

Here, the physical field $g^{\text{phys}}(\mathbf{r}, t)$ is simply obtained as the real part of the complex-valued field $g(\mathbf{r}, t)$. Note that both the 0th-order term $g_0(\mathbf{r})$ and the time-averaged 2nd-order terms $g_2(\mathbf{r})$ are real-valued and time independent. The time average $\langle \dots \rangle$ is defined over a full oscillation period $\tau_0 = 2\pi/\omega$, and the time average of a product of two 1st-order fields is easily computed using the complex-valued fields,

$$\langle g^{\text{phys}}(\mathbf{r}, t) \rangle = \frac{1}{\tau_0} \int_0^{\tau_0} g^{\text{phys}}(\mathbf{r}, t) dt, \quad (2a)$$

$$\langle A_1^{\text{phys}}(\mathbf{r}, t) B_1^{\text{phys}}(\mathbf{r}, t) \rangle = \frac{1}{2} \text{Re}[A_1(\mathbf{r}) B_1^*(\mathbf{r})], \quad (2b)$$

where the asterisk denotes complex conjugation.

A. The linear isotropic elastic solid

We assume that the solid domain Ω^{sl} contains a linear elastic solid with density ρ^{sl} , where the position \mathbf{r} of a solid element with equilibrium position \mathbf{r}_0 is given in terms of the Lagrangian displacement field $\mathbf{u} = \mathbf{u}_1$ as

$$\mathbf{r}(\mathbf{r}_0) = \mathbf{r}_0 + \mathbf{u}_1(\mathbf{r}_0) e^{-i\omega t}, \quad \text{for } \mathbf{r}_0 \in \Omega^{\text{sl}}. \quad (3)$$

This is a 1st-order expression, since the steady time-averaged 2nd-order displacement \mathbf{u}_2 is neglected as the steady pressure p_2 in the fluid is too small to deform the surrounding solid noticeably. Using index notation, the governing equation for \mathbf{u}_1 is given by the Cauchy momentum equation in terms of the elastic moduli C_{ik} and the stress tensor σ_1^{sl} with components σ_{1ik}^{sl} [39],

$$u_{1i} = -\frac{1}{\omega^2 \rho^{\text{sl}}} \partial_k \sigma_{1ik}^{\text{sl}}, \quad \text{for } \mathbf{r}_0 \in \Omega^{\text{sl}}, \quad (4a)$$

$$\sigma_{1ik}^{\text{sl}} = C_{44}(\partial_i u_{1k} + \partial_k u_{1i}) + (C_{11} - 2C_{44})\partial_j u_{1j} \delta_{ik}. \quad (4b)$$

At the fluid-solid interface $\partial\Omega_{\text{sl}}^{\text{fl}}$, the equilibrium position is denoted \mathbf{s}_0 , and the interface displacement and velocity is $\mathbf{s}_1 = \mathbf{u}_1(\mathbf{s}_0)$ and $\mathbf{V}_1^0 = \partial_t \mathbf{s}_1$, respectively,

$$\mathbf{s}(\mathbf{s}_0, t) = \mathbf{s}_0 + \mathbf{s}_1(\mathbf{s}_0) e^{-i\omega t}, \quad \text{for } \mathbf{s}_0 \in \partial\Omega_{\text{sl}}^{\text{fl}}, \quad (5a)$$

$$\partial_t \mathbf{s}(\mathbf{s}_0, t) = -i\omega \mathbf{s}_1(\mathbf{s}_0) e^{-i\omega t} = \mathbf{V}_1^0(\mathbf{s}_0) e^{-i\omega t}. \quad (5b)$$

The boundary conditions on $\partial\Omega_{\text{sl}}^{\text{fl}}$ follows from Eq. (5b), and they are treated further in Sec. II C. The remaining part of $\partial\Omega^{\text{sl}}$ is divided into the free surface $\Omega_{\text{free}}^{\text{sl}}$ and the transducer-solid interface $\Omega_{\text{sl}}^{\text{pz}}$,

$$\sigma_1^{\text{sl}} \cdot \mathbf{n} = \sigma_1^{\text{fl}} \cdot \mathbf{n} \quad \text{and} \quad \mathbf{V}_1^0 = \mathbf{v}_1, \quad \text{for } \mathbf{r} \in \partial\Omega_{\text{sl}}^{\text{fl}}, \quad (6a)$$

$$\sigma_1^{\text{sl}} \cdot \mathbf{n} = \sigma_1^{\text{pz}} \cdot \mathbf{n} \quad \text{and} \quad \mathbf{u}_1^{\text{sl}} = \mathbf{u}_1^{\text{pz}}, \quad \text{for } \mathbf{r} \in \partial\Omega_{\text{sl}}^{\text{pz}}, \quad (6b)$$

$$\sigma_1^{\text{sl}} \cdot \mathbf{n} = \mathbf{0}, \quad \text{for } \mathbf{r} \in \partial\Omega_{\text{free}}^{\text{sl}}. \quad (6c)$$

B. The linear piezoelectric transducer

The linear piezoelectric transducer is described by the elastic deformation \mathbf{u}_1 and the electric potential φ_1 governed by the Cauchy momentum equation and the zero-free-charge Gauss's law for dielectrics coupled by the constitutive equations $\sigma_1^{\text{pz}}(\mathbf{u}_1, \varphi_1)$ and $\mathbf{D}_1(\mathbf{u}_1, \varphi_1)$ for the mechanical stress and electric displacement, respectively, presented in Appendix A,

$$-\rho^{\text{pz}} \omega^2 \mathbf{u}_1 = \nabla \cdot \sigma_1^{\text{pz}}(\mathbf{u}_1, \varphi_1), \quad (7a)$$

$$\mathbf{0} = \nabla \cdot \mathbf{D}_1(\mathbf{u}_1, \varphi_1), \quad (7b)$$

where $\sigma_1^{\text{pz}}(\mathbf{u}_1, \varphi_1)$ and $\mathbf{D}_1(\mathbf{u}_1, \varphi_1)$ are given in Eq. (A2).

The boundary $\partial\Omega^{\text{pz}}$ of Ω^{pz} is divided into three parts: the interface $\Omega_{\text{sl}}^{\text{pz}}$ between Ω^{pz} and Ω^{sl} , the interface $\Omega_{\text{el},n}^{\text{pz}}$

between Ω^{pz} and the n solid electrodes, and the free surface $\Omega_{\text{free}}^{\text{pz}}$. The boundary conditions on each part are

$$\sigma_1^{\text{pz}} \cdot \mathbf{n} = \sigma_1^{\text{sl}} \cdot \mathbf{n}, \quad \mathbf{u}_1^{\text{pz}} = \mathbf{u}_1^{\text{sl}}, \quad \text{and} \quad \varphi_1 = \varphi_0^{(n)}, \quad \text{for } \mathbf{r} \in \partial\Omega_{\text{el},n}^{\text{pz}}, \quad (8a)$$

$$\sigma_1^{\text{pz}} \cdot \mathbf{n} = \sigma_1^{\text{sl}} \cdot \mathbf{n}, \quad \mathbf{u}_1^{\text{pz}} = \mathbf{u}_1^{\text{sl}}, \quad \text{and} \quad \mathbf{n} \cdot \mathbf{D}_1 = 0, \quad \text{for } \mathbf{r} \in \partial\Omega_{\text{sl}}^{\text{pz}}, \quad (8b)$$

$$\sigma_1^{\text{pz}} \cdot \mathbf{n} = \mathbf{0} \quad \text{and} \quad \mathbf{n} \cdot \mathbf{D}_1 = 0, \quad \text{for } \mathbf{r} \in \partial\Omega_{\text{free}}^{\text{pz}}. \quad (8c)$$

C. The Newtonian fluid

We assume that the fluid domain Ω^{fl} contains a Newtonian fluid described by the Eulerian fields density ρ , pressure p , and velocity \mathbf{v} , and by the parameters of the unperturbed state: density ρ_0 , sound speed c_0 , compressibility $\kappa_0 = 1/(\rho_0 c_0^2)$, dynamic viscosity η_0 , and bulk viscosity η_0^{b} . The governing equations in the adiabatic limit are the continuity and momentum equation,

$$\partial_t \rho = -\nabla \cdot (\rho \mathbf{v}), \quad (9a)$$

$$\partial_t (\rho \mathbf{v}) = -\nabla \cdot [(\rho \mathbf{v}) \mathbf{v}] + \nabla \cdot \sigma^{\text{fl}}, \quad (9b)$$

where σ^{fl} is the stress tensor with components σ_{ik}^{fl} ,

$$\sigma_{ik}^{\text{fl}} = [-p + (\eta_0^{\text{b}} - \frac{2}{3}\eta_0)\partial_j v_j] \delta_{ik} + \eta_0(\partial_i v_k + \partial_k v_i). \quad (9c)$$

In contrast to the solid domain, the governing equations in the fluid domain are nonlinear, and thus we include the 2nd-order time-averaged fields in the perturbation expansion,

$$\rho = \rho_0 + \rho_1(\mathbf{r}) e^{-i\omega t} + \rho_2(\mathbf{r}), \quad (10a)$$

$$p = p_0 + p_1(\mathbf{r}) e^{-i\omega t} + p_2(\mathbf{r}), \quad (10b)$$

$$\mathbf{v} = \mathbf{0} + \mathbf{v}_1(\mathbf{r}) e^{-i\omega t} + \mathbf{v}_2(\mathbf{r}), \quad \text{for } \mathbf{r} \in \Omega^{\text{fl}}. \quad (10c)$$

The resulting governing equations for 1st- and 2nd-order perturbation are presented in respectively Secs. III and IV below, but already here, we follow up on Eq. (5) and formulate the no-slip boundary condition (no-slip BC) $\mathbf{v} = \partial_t \mathbf{s}$ relating the Eulerian fluid velocity \mathbf{v} to the Lagrangian wall velocity $\partial_t \mathbf{s}$ Eq. (5b) at the fluid-solid interface $\partial\Omega_{\text{sl}}^{\text{fl}}$. This condition applies at all times at the actual position $\mathbf{s}(\mathbf{s}_0, t)$ Eq. (5a), so we obtain

$$\mathbf{v}(\mathbf{s}_0 + \mathbf{s}_1 e^{-i\omega t}, t) = \mathbf{V}_1^0(\mathbf{s}_0) e^{-i\omega t}, \quad \text{no-slip BC.} \quad (11)$$

Combining Eqs. (10c) and (11) with the Taylor expansion $\mathbf{v}(\mathbf{s}_0 + \mathbf{s}_1, t) \approx \mathbf{v}_1(\mathbf{s}_0) e^{-i\omega t} + \langle (\mathbf{s}_1 \cdot \nabla) \mathbf{v}_1 \rangle|_{\mathbf{s}_0}$, and collecting the terms order by order, gives

$$\mathbf{v}_1(\mathbf{s}_0) = \mathbf{V}_1^0(\mathbf{s}_0), \quad \text{1st-order no-slip BC,} \quad (12a)$$

$$\mathbf{v}_2(\mathbf{s}_0) = -\langle (\mathbf{s}_1 \cdot \nabla) \mathbf{v}_1 \rangle|_{\mathbf{s}_0}, \quad \text{2nd-order no-slip BC.} \quad (12b)$$

D. Surface, boundary-layer, and bulk fields for weakly-curved fluid-solid interfaces

A central quantity in acoustofluidic theory, is the so-called boundary-layer thickness δ , which is a dynamically defined length scale that appears in the acoustically oscillating fluid inside Ω^{fl} near the fluid-solid interface $\partial\Omega_{\text{sl}}^{\text{fl}}$, see Sec. III. For MHz-ultrasound in water, $\delta \approx 0.5 \mu\text{m}$ is very small compared to the inverse wave number $k_0^{-1} = c_0/\omega \approx 240 \mu\text{m}$, and for weakly curved surfaces it is also much smaller than the radius of curvature R of $\partial\Omega_{\text{sl}}^{\text{fl}}$,

$$\delta = \sqrt{\frac{2\nu_0}{\omega}}, \quad \text{small boundary length scale,} \quad (13a)$$

$$d = \min\left\{\frac{c_0}{\omega}, R\right\}, \quad \text{large bulk length scale,} \quad (13b)$$

$$\epsilon = \frac{\delta}{d} \ll 1, \quad \text{small length-scale ratio.} \quad (13c)$$

As in BL18, we introduce for a given point \mathbf{s}_0 at $\partial\Omega_{\text{sl}}^{\text{fl}}$ the orthonormal local coordinates ξ , η , and ζ with their origin at \mathbf{s}_0 , such that ζ is the normal coordinate pointing into Ω^{fl} , $\mathbf{e}_\zeta = -\mathbf{n}(\partial\Omega_{\text{sl}}^{\text{fl}})$, and ξ and η are the coordinates in the tangent plane to $\partial\Omega_{\text{sl}}^{\text{fl}}$ at \mathbf{s}_0 with $\mathbf{e}_\xi \times \mathbf{e}_\eta = \mathbf{e}_\zeta$.

Importantly, for fluid fields both in 1st- and in 2nd-order perturbation, we distinguish between bulk fields \mathbf{A}^d that extend into the bulk with spatial variation on the bulk length scale d and that are typically found by numerical simulation, and boundary-layer fields \mathbf{A}^δ that decays to zero away from the wall on the boundary-layer length scale δ . For the boundary-layer fields, the smallness of the length ratio $\epsilon \sim \delta/d$ allows for separation of variables and simplification of the differential geometrical properties, as summarized in the following expressions, where superscript '0' refers to surface properties that only depends on the in-plane coordinates ξ and η , and where subscript "||" denotes tangential components,

$$\mathbf{A}^\delta(\xi, \eta, \zeta) \approx \mathbf{A}^{\delta 0}(\xi, \eta) a^\delta(\zeta), \quad (14a)$$

$$\text{with } a^\delta(\zeta) \rightarrow 0 \text{ for } \frac{\zeta}{\delta} \rightarrow \infty.$$

$$\mathbf{A}_{||} = A_\xi \mathbf{e}_\xi + A_\eta \mathbf{e}_\eta, \quad (14b)$$

$$\nabla_{||} = \mathbf{e}_\xi \partial_\xi + \mathbf{e}_\eta \partial_\eta, \quad (14c)$$

$$\nabla \cdot \mathbf{A}^0 \approx \nabla_{||} \cdot \mathbf{A}_{||}^0, \quad (14d)$$

$$\mathbf{A}^0 \cdot \nabla \mathbf{B}^0 \approx \mathbf{A}_{||}^0 \cdot (\nabla_{||} \mathbf{B}_{||}^0) \mathbf{e}_i, \quad (14e)$$

$$\nabla^2 a^\delta \approx \partial_\zeta^2 a^\delta, \quad (14f)$$

$$\nabla^2 \mathbf{A}^\delta \approx \mathbf{A}^{\delta 0} \partial_\zeta^2 a(\zeta) = \partial_\zeta^2 \mathbf{A}^\delta, \quad (14g)$$

$$\nabla \cdot \mathbf{A}^\delta \approx \nabla_{||} \cdot \mathbf{A}_{||}^\delta + \partial_\zeta A_\zeta^\delta. \quad (14h)$$

III. 1ST-ORDER ACOUSTIC FLUID FIELDS

The first step in developing the governing equations (9) for a Newtonian fluid in a 1st-order time-harmonic per-

turbation expansion (10), is to use the adiabatic relation between the pressure p_1 and the density ρ_1 ,

$$i\omega\kappa_0 p_1 = \nabla \cdot \mathbf{v}_1, \quad \text{with } p_1 = c_0^2 \rho_1, \quad (15a)$$

$$-i\omega\rho_0 \mathbf{v}_1 = \nabla \cdot \boldsymbol{\sigma}_1^{\text{fl}}, \quad (15b)$$

where the 1st-order stress $\boldsymbol{\sigma}_1^{\text{fl}}$ is given by Eq. (9c) upon substituting p and \mathbf{v} by p_1 and \mathbf{v}_1 , respectively. We have no changes to the treatment in the BL18 model of the 1st-order acoustic fields, so this section contains just a brief summary. The second step is to perform a Helmholtz decomposition of the velocity field \mathbf{v}_1 into a curl-free compressible potential-flow component \mathbf{v}_1^d and a divergence-free incompressible component \mathbf{v}_1^δ ,

$$\mathbf{v}_1 = \mathbf{v}_1^d + \mathbf{v}_1^\delta, \quad (16)$$

$$\text{with } \nabla \times \mathbf{v}_1^d = \mathbf{0} \text{ and } \nabla \cdot \mathbf{v}_1^\delta = 0.$$

Using these expressions, \mathbf{v}_1^δ decouples from \mathbf{v}_1^d , p_1 , and ρ_1 , and drops out of the continuity equation, \mathbf{v}_1^d is proportional to ∇p_1 , and the governing equations for p_1 and \mathbf{v}_1^δ reduce to Helmholtz equations with the weakly damped compression wave number k_c and the strongly damped shear wave number k_s , respectively,

$$\mathbf{v}_1^d = -i \frac{1 - i\Gamma}{\omega\rho_0} \nabla p_1, \quad \text{with } \Gamma = \frac{(1+\beta)\eta_0\omega}{\rho_0 c_0^2}, \quad (17a)$$

$$\nabla \cdot \mathbf{v}_1^d = i\omega\kappa_0 p_1, \quad \text{with } \beta = \frac{\eta_0^b}{\eta_0} + \frac{1}{3}, \quad (17b)$$

$$\nabla^2 p_1 = -k_c^2 p_1, \quad \text{with } k_c = \left(1 + i\frac{\Gamma}{2}\right)k_0, \quad k_0 = \frac{\omega}{c_0}, \quad (17c)$$

$$\nabla^2 \mathbf{v}_1^\delta = -k_s^2 \mathbf{v}_1^\delta, \quad \text{with } k_s = \frac{1+i}{\delta}, \quad \delta = \sqrt{\frac{2\nu_0}{\omega}}. \quad (17d)$$

We note that it is through the Helmholtz equation (17d) with its exponentially decaying solutions due to the shear wave number k_s that the notion of boundary layers of width δ enters the theory. We also note that the damping coefficient Γ in the compression wave number k_c is of second order in the small parameter ϵ of Eq. (13c), $\Gamma = \frac{1}{2}(1+\beta)\epsilon^2 \ll 1$, indeed a weak damping.

Although of second order, the average acoustic energy density E_{ac} of the fluid occupying the volume V_{fl} and the time-averaged acoustic radiation force \mathbf{F}^{rad} on a suspended particle of radius a and scattering coefficients f_0 and f_1 , are given directly by the 1st-order fields as [20],

$$E_{\text{ac}} = \frac{1}{V_{\text{fl}}} \int_{V_{\text{fl}}} \left[\frac{1}{4}\kappa_0 |p_1|^2 + \frac{1}{4}\rho_0 |\mathbf{v}_1|^2 \right] dV, \quad (18a)$$

$$\mathbf{F}^{\text{rad}} = \pi a^3 \nabla \left[\frac{1}{3} f_0 \kappa_0 |p_1|^2 - \frac{1}{2} f_1 \frac{1}{4} \rho_0 |\mathbf{v}_1|^2 \right]. \quad (18b)$$

A. The analytical 1st-order boundary-layer field

For weakly curved, thin boundary layers, discussed in Sec. IID, the analytical form of the incompressible veloc-

ity field \mathbf{v}_1^δ is easily found from Eq. (17d) to be

$$\mathbf{v}_1^\delta = \mathbf{v}_1^{\delta 0}(\xi, \eta) e^{ik_s \zeta} + \mathcal{O}(\epsilon), \quad (19a)$$

$$\mathbf{v}_1^{\delta 0} = \mathbf{V}_1^0 - \mathbf{v}_1^{d0}, \text{ 1st-order no-slip BC.} \quad (19b)$$

Here, by combining Eqs. (12) and (16), the amplitude $\mathbf{v}_1^{\delta 0}(\xi, \eta)$ of \mathbf{v}_1^δ on the surface $\zeta = 0$ is expressed as the difference between the oscillation velocity $\mathbf{V}_1^0(\xi, \eta)$ of the wall and the value $\mathbf{v}_1^{d0}(\xi, \eta)$ of the compressible (acoustic) velocity field \mathbf{v}_1^d at the surface. Note how $\mathbf{v}_1^\delta = \mathbf{v}_1^{\delta 0} e^{i\zeta/\delta} e^{-\zeta/\delta}$ decays exponentially on the small length scale δ in the ζ -direction normal to the wall.

B. Boundary condition for the 1st-order pressure

A crucial relation in the BL18 model, is the expression for the normal component $v_{1\zeta}^{\delta 0}$ of $\mathbf{v}_1^{\delta 0}$ on the surface in terms of the wall velocity \mathbf{V}_1^0 and the bulk acoustic velocity \mathbf{v}_1^{d0} , which follows from the incompressibility condition (16) and the analytical form (19),

$$v_{1\zeta}^{\delta 0} = \frac{i}{k_s} \nabla_{\parallel} \cdot \mathbf{v}_{1\parallel}^{\delta 0} = \frac{i}{k_s} \nabla_{\parallel} \cdot \mathbf{V}_{1\parallel}^0 - \frac{i}{k_s} \nabla_{\parallel} \cdot \mathbf{v}_{1\parallel}^{d0}. \quad (20)$$

Using this result, the boundary condition $v_{1\zeta}^{d0} = V_{1\zeta}^0 - v_{1\zeta}^{\delta 0}$ for the bulk field at the surface takes the self-consistent form to leading order in $\delta = (1+i)/k_s$.

$$v_{1\zeta}^{d0} = \left(V_{1\zeta}^0 - \frac{i}{k_s} \nabla_{\parallel} \cdot \mathbf{V}_{1\parallel}^0 \right) + \frac{i}{k_s} \nabla_{\parallel} \cdot \mathbf{v}_{1\parallel}^{d0}. \quad (21)$$

Writing this 1st-order velocity boundary condition (BC) in terms of the pressure p_1 , using $\nabla_{\parallel} \cdot \mathbf{v}_{1\parallel}^{d0} = \nabla \cdot \mathbf{v}_1^{d0} - \partial_{\zeta} v_{1\zeta}^{d0}$ and Eq. (17a), leads to the self-consistent boundary condition for the 1st-order pressure p_1 in the BL18 model,

$$\partial_{\zeta} p_1 = \frac{i\omega\rho_0}{1-i\Gamma} \left(V_{1\zeta}^0 - \frac{i}{k_s} \nabla_{\parallel} \cdot \mathbf{V}_{1\parallel}^0 \right) - \frac{i}{k_s} \left(k_c^2 p_1 + \partial_{\zeta}^2 p_1 \right), \quad (22)$$

1st-order pressure BC at Ω^{fl} .

C. Boundary condition for the 1st-order stress

The 1st-order stress condition $\boldsymbol{\sigma}^{\text{sl}} \cdot \mathbf{e}_{\zeta} = \boldsymbol{\sigma}_1^{\text{fl}} \cdot \mathbf{e}_{\zeta}$ at the interface $\partial\Omega_{\text{sl}}^{\text{fl}}$ with inward surface normal \mathbf{e}_{ζ} , is rewritten by combining the 1st-order part $\boldsymbol{\sigma}_1^{\text{fl}}$ of $\boldsymbol{\sigma}^{\text{fl}}$ Eq. (9c) with the 1st-order expressions Eqs. (16), (17) and (19). Keeping terms to leading order in $k_0\delta$ leads to the 1st-order stress boundary condition of the BL18 model,

$$\begin{aligned} \boldsymbol{\sigma}_1^{\text{sl}} \cdot \mathbf{e}_{\zeta} &= -p_1 \mathbf{e}_{\zeta} + ik_s \eta_0 \left(\mathbf{V}_{1\parallel}^0 - \mathbf{v}_{1\parallel}^{d0} \right) \\ &\quad + ik_s \eta_0 2 \left(V_{1\zeta}^0 - v_{1\zeta}^{d0} \right) \mathbf{e}_{\zeta}, \\ &= -p_1 \mathbf{e}_{\zeta} + ik_s \eta_0 \left[\mathbf{V}^0 - \mathbf{v}_1^d + (V_{1\zeta}^0 - v_{1\zeta}^{d0}) \mathbf{e}_{\zeta} \right], \end{aligned} \quad (23)$$

1st-order stress BC at Ω^{fl} ,

where in the last expression have used $\mathbf{v} = \mathbf{v}_{\parallel} + v_{\zeta} \mathbf{e}_{\zeta}$. Since $k_s \eta_0 = \frac{1+i}{\delta} \eta_0 = \frac{1+i}{2} k_0 \delta \rho_0 c_0$, Eq. (23) is the usual pressure condition plus a correction term of order $k_0\delta = \epsilon$ due to the viscous stress $\eta_0 \partial_{\zeta} \mathbf{v}_1^{\delta}$ in the boundary layer. The last term in Eq. (23) was left out in the BL18 model.

IV. 2ND-ORDER TIME-AVERAGED STREAMING FIELDS IN THE FLUID

We compute the time-averaged acoustic streaming by 2nd-order perturbation theory, closely following the BL18 model but now extending it in the BL25 model by keeping terms of higher-order in $k_0\delta$ hitherto neglected. The time-averaged part of the governing equations and the boundary conditions in 2nd-order perturbation are obtained from Eqs. (9) and (12),

$$\rho_0 \nabla \cdot \mathbf{v}_2 = -\nabla \cdot \langle \rho_1, \mathbf{v}_1 \rangle, \quad (24a)$$

$$\nabla \cdot \boldsymbol{\sigma}_2^{\text{fl}} = \rho_0 \nabla \cdot \langle \mathbf{v}_1, \mathbf{v}_1 \rangle, \quad (24b)$$

$$\mathbf{v}_2^0 = -\frac{1}{\omega} \langle i\mathbf{v}_1^0 \cdot \nabla, \mathbf{v}_1^0 \rangle, \quad (24c)$$

where we have followed Eq. (10) and dropped $\langle \cdot \rangle$ from the time-averaged velocity \mathbf{v}_2 , pressure p_2 , and stress $\boldsymbol{\sigma}_2^{\text{fl}}$. Equation (24) is a compressible Stokes flow problem in the 2nd-order fields \mathbf{v}_2 and $\boldsymbol{\sigma}_2^{\text{fl}}$, where the known 1st-order fields act as source terms. This problem is split in two parts: the 2nd-order boundary-layer fields driven by the short-range source terms $\nabla \cdot \langle \rho_1 \mathbf{v}_1^{\delta} \rangle$ and $\rho_0 \nabla \cdot \langle \mathbf{v}_1^{\delta} \mathbf{v}_1^{\delta} + \mathbf{v}_1^{\delta} \mathbf{v}_1^d + \mathbf{v}_1^d \mathbf{v}_1^{\delta} \rangle$, and the 2nd-order bulk streaming field driven by the long-range source terms, $\nabla \cdot \langle \rho_1 \mathbf{v}_1^d \rangle$ and $\rho_0 \nabla \cdot \langle \mathbf{v}_1^d \mathbf{v}_1^d \rangle$. The corresponding responses are long-range bulk fields (superscript “d”) and short-range boundary-layer fields (superscript “ δ ”),

$$\mathbf{v}_2 = \mathbf{v}_2^d + \mathbf{v}_2^{\delta}, \quad \text{for } \mathbf{r} \in \partial\Omega_{\text{sl}}^{\text{fl}}, \quad (25a)$$

$$p_2 = p_2^d + p_2^{\delta}, \quad \text{for } \mathbf{r} \in \partial\Omega_{\text{sl}}^{\text{fl}}, \quad (25b)$$

$$\boldsymbol{\sigma}_2^{\text{fl}} = \boldsymbol{\sigma}_2^d + \boldsymbol{\sigma}_2^{\delta}, \quad \text{for } \mathbf{r} \in \partial\Omega_{\text{sl}}^{\text{fl}}, \quad (25c)$$

$$\mathbf{v}_2^{d0} = -\mathbf{v}_2^{\delta 0} - \langle (\mathbf{s}_1 \cdot \nabla) \mathbf{v}_1 \rangle, \quad \text{for } \mathbf{r} = \mathbf{s}_0. \quad (25d)$$

A. Short-range boundary-layer streaming

The governing equations for the 2nd-order boundary-layer fields, \mathbf{v}_2^{δ} , p_2^{δ} , and $\boldsymbol{\sigma}_2^{\delta}$, are obtained by collecting the terms of Eq. (24) which contains at least one short-range 1st-order field \mathbf{v}_1^{δ} ,

$$\nabla \cdot (\rho_0 \mathbf{v}_2^{\delta}) = -\nabla \cdot \langle \rho_1 \mathbf{v}_1^{\delta} \rangle, \quad (26a)$$

$$\nabla \cdot \boldsymbol{\sigma}_2^{\delta} = \rho_0 \nabla \cdot \langle \mathbf{v}_1^{\delta} \mathbf{v}_1^{\delta} + \mathbf{v}_1^{\delta} \mathbf{v}_1^d + \mathbf{v}_1^d \mathbf{v}_1^{\delta} \rangle, \quad (26b)$$

$$\text{with } \nabla \cdot \boldsymbol{\sigma}_2^{\delta} = \nabla \cdot (-p_2^{\delta} + \beta \eta_0 \nabla \cdot \mathbf{v}_2^{\delta}) + \eta_0 \nabla^2 \mathbf{v}_2^{\delta}, \quad (26c)$$

$$\text{where } \mathbf{v}_2^{\delta} \rightarrow \mathbf{0} \text{ and } p_2^{\delta} \rightarrow 0 \text{ as } \zeta \rightarrow \infty. \quad (26d)$$

Thus \mathbf{v}_2^{δ} , p_2^{δ} , and $\boldsymbol{\sigma}_2^{\delta}$ are driven by source terms containing time-average products of 1st-order terms of the form

$\langle \mathbf{A}_1, \mathbf{B}_1 \rangle$, where \mathbf{A}_1 and \mathbf{B}_1 are either \mathbf{v}_1^d or \mathbf{v}_1^δ . To solve Eq. (26), we first combine Eq. (26b) and Eq. (26c) to obtain the Laplacian of \mathbf{v}_2^δ ,

$$\eta_0 \nabla^2 \mathbf{v}_2^\delta = -\beta \eta_0 \nabla(\nabla \cdot \mathbf{v}_2^\delta) + \nabla p_2^\delta + \rho_0 \nabla \cdot \langle \mathbf{v}_1^\delta \mathbf{v}_1^\delta + \mathbf{v}_1^d \mathbf{v}_1^\delta + \mathbf{v}_1^\delta \mathbf{v}_1^d \rangle. \quad (27)$$

We note that Eq. (14f) gives $\nabla^2 \mathbf{v}_2^\delta \approx \partial_\zeta^2 \mathbf{v}_2^\delta$, and that using Eq. (26a) the divergence term is rewritten as $-\beta \eta_0 \nabla(\nabla \cdot \mathbf{v}_2^\delta) = \beta \nu_0 \nabla \langle \mathbf{v}_1^\delta \cdot \nabla \rho_1 \rangle = \frac{\beta \eta_0 \omega}{c_0^2} \nabla \langle \mathbf{v}_1^\delta \cdot (\mathbf{i} \mathbf{v}_1^d) \rangle$. This term is neglected as it is smaller by a factor Γ compared to the other divergence term. In the BL18 model, the short-range 2nd-order pressure field p_2^δ was also neglected since the perpendicular velocity of the wall was assumed to be small. However, a major point in the BL25 model is that we relax this assumption and keep p_2^δ . Thus, we end with two source terms for \mathbf{v}_2^δ , which therefore is split in two corresponding terms,

$$\mathbf{v}_2^\delta = \mathbf{v}_2^{\delta p} + \mathbf{v}_2^{\delta v}, \quad (28a)$$

$$\text{where } \mathbf{v}_2^{\delta p}(\xi, \eta, \infty) = \mathbf{v}_2^{\delta v}(\xi, \eta, \infty) = \mathbf{0},$$

$$\partial_\zeta^2 \mathbf{v}_2^{\delta p} = \frac{1}{\eta_0} \nabla p_2^\delta, \quad (28b)$$

$$\partial_\zeta^2 \mathbf{v}_2^{\delta v} = \frac{1}{\nu_0} \nabla \cdot \langle \mathbf{v}_1^\delta \mathbf{v}_1^\delta + \mathbf{v}_1^d \mathbf{v}_1^\delta + \mathbf{v}_1^\delta \mathbf{v}_1^d \rangle. \quad (28c)$$

An analytical expression for \mathbf{v}_2^δ is derived by separating the 1st-order fields in the source terms into the parallel coordinates (ξ, η) and the perpendicular coordinate ζ ,

$$\mathbf{A}_1 = a(\zeta) \mathbf{A}_1^0(\xi, \eta), \quad (29a)$$

$$\mathbf{B}_1 = b(\zeta) \mathbf{B}_1^0(\xi, \eta), \quad (29b)$$

$$\langle \mathbf{A}_1, \mathbf{B}_1 \rangle = \langle a \mathbf{A}_1^0, b \mathbf{B}_1^0 \rangle = \langle ab^* \mathbf{A}_1^0, \mathbf{B}_1^0 \rangle, \quad (29c)$$

$$\text{with } \langle A_1, B_1 \rangle = \langle A_1 B_1 \rangle,$$

where in the last expression, we have introduced the comma-separated notation $\langle A_1, B_1 \rangle = \langle A_1 B_1 \rangle$ to ensure clarity when moving pre-factors back and forth between A_1^0 and B_1^0 , such as when collecting all ζ -dependence in the product $a(\zeta)b^*(\zeta)$. The appearance of the simplified Laplacian (14f), $\nabla^2 g^\delta \approx \partial_\zeta^2 g^\delta$, in the boundary-layer equations (26), implies, that we need to integrate terms $\langle \mathbf{A}_1, \mathbf{B}_1 \rangle$ with respect to ζ . To this end, as in the BL18 model, we introduce the recursive n -fold integrals $I_{ab}^{(n)}(\zeta)$ for integer values $n = 1, 2, 3, \dots$, and for the extensions $n = 0$ (no integration) and $-n$ (the n th derivative),

$$I_{ab}^{(0)}(\zeta) = a(\zeta) b(\zeta)^*, \quad \lim_{\zeta \rightarrow \infty} [a(\zeta) b(\zeta)^*] \rightarrow 0, \quad (30a)$$

$$I_{ab}^{(n)}(\zeta) = \int_\infty^\zeta d\zeta_n I_{ab}^{(n-1)}(\zeta_n), \quad n = 1, 2, 3, \dots, \quad (30b)$$

$$I_{ab}^{(-n)}(\zeta) = \partial_\zeta^n [a(\zeta) b(\zeta)^*], \quad n = 1, 2, 3, \dots, \quad (30c)$$

$$I_{ba}^{(n)}(\zeta) = [I_{ab}^{(n)}(\zeta)]^*, \quad \pm n = 0, 1, 2, 3, \dots, \quad (30d)$$

$$\langle \mathbf{A}_1, \mathbf{B}_1 \rangle = \langle I_{ab}^{(0)}(\zeta) \mathbf{A}_1^0(\xi, \eta), \mathbf{B}_1^0(\xi, \eta) \rangle. \quad (30e)$$

We also need the coordinate-separated expressions for the i th component $[\nabla \cdot \langle \mathbf{A}_1, \mathbf{B}_1 \rangle]_i$ of the single-divergence $\nabla \cdot \langle \mathbf{A}_1, \mathbf{B}_1 \rangle$,

$$[\nabla \cdot \langle \mathbf{A}_1, \mathbf{B}_1 \rangle]_i = \nabla \cdot \langle I_{ab}^{(0)}(\zeta) \mathbf{A}_{1i}^0, \mathbf{B}_1^0 \rangle \quad (31a)$$

$$= \nabla_\parallel \cdot \langle (I_{ab}^{(0)}(\zeta) \mathbf{A}_{1i}^0, \mathbf{B}_{1\parallel}^0) \rangle + \langle I_{ab}^{(-1)}(\zeta) \mathbf{A}_{1i}^0, \mathbf{B}_{1\zeta}^0 \rangle.$$

with tangential and normal components

$$[\nabla \cdot \langle \mathbf{A}_1, \mathbf{B}_1 \rangle]_\parallel \quad (31b)$$

$$= \nabla_\parallel \cdot \langle (I_{ab}^{(0)}(\zeta) \mathbf{A}_{1\parallel}^0, \mathbf{B}_{1\parallel}^0) \rangle + \langle I_{ab}^{(-1)}(\zeta) \mathbf{A}_{1\parallel}^0, \mathbf{B}_{1\zeta}^0 \rangle,$$

$$[\nabla \cdot \langle \mathbf{A}_1, \mathbf{B}_1 \rangle]_\zeta \quad (31c)$$

$$= \nabla_\parallel \cdot \langle (I_{ab}^{(0)}(\zeta) \mathbf{A}_{1\zeta}^0, \mathbf{B}_{1\parallel}^0) \rangle + \langle I_{ab}^{(-1)}(\zeta) \mathbf{A}_{1\zeta}^0, \mathbf{B}_{1\zeta}^0 \rangle,$$

and for the double-divergence $\nabla \cdot [\nabla \cdot \langle \mathbf{A}_1, \mathbf{B}_1 \rangle]$,

$$\nabla \cdot [\nabla \cdot \langle \mathbf{A}_1, \mathbf{B}_1 \rangle] \quad (31d)$$

$$= \partial_i [\nabla_\parallel \cdot \langle (I_{ab}^{(0)}(\zeta) \mathbf{A}_{1i}^0, \mathbf{B}_{1\parallel}^0) \rangle + \langle I_{ab}^{(-1)}(\zeta) \mathbf{A}_{1i}^0, \mathbf{B}_{1\zeta}^0 \rangle]$$

$$= \nabla_\parallel \cdot [\nabla_\parallel \cdot \langle I_{ab}^{(0)}(\zeta) \mathbf{A}_{1\parallel}^0, \mathbf{B}_{1\parallel}^0 \rangle] + \langle I_{ab}^{(-2)}(\zeta) \mathbf{A}_{1\zeta}^0, \mathbf{B}_{1\zeta}^0 \rangle$$

$$+ \nabla_\parallel \cdot [\langle I_{ab}^{(-1)}(\zeta) \mathbf{A}_{1\parallel}^0, \mathbf{B}_{1\zeta}^0 \rangle + \langle I_{ab}^{(-1)}(\zeta) \mathbf{A}_{1\zeta}^0, \mathbf{B}_{1\parallel}^0 \rangle].$$

Using the solution (19a) for \mathbf{v}_1^δ and a 1st-order Taylor-expansion in ζ of \mathbf{v}_1^d valid in the boundary layer $\zeta \ll d$, we obtain the explicit coordinate-separated form for the relevant velocity fields in the boundary layer,

$$\mathbf{v}_1^\delta = q(\zeta) \mathbf{v}_1^{\delta 0}(\xi, \eta), \quad \text{with } q(\zeta) = e^{ik_s \zeta}, \quad (32a)$$

$$\mathbf{v}_1^d = \mathbf{v}_1^{d0} + \zeta \partial_\zeta \mathbf{v}_1^{d0}, \quad \text{with } \partial_\zeta \mathbf{v}_1^{d0} = \lim_{\zeta \rightarrow 0} \partial_\zeta \mathbf{v}_1^d. \quad (32b)$$

We now see that the functions $a(\zeta)$ and $b(\zeta)$ of Eq. (29) in the source terms of Eq. (26) are either $q(\zeta)$, ζ , or unity, and that each product $a(\zeta)b(\zeta)$ contains at least one decaying factor $q(\zeta)$, so the zero-at-infinity boundary condition (30a) is fulfilled. On the surface $\zeta = 0$, $I_{ab}^{(n)}(\zeta)$ becomes $\hat{I}_{ab}^{(n)} = I_{ab}^{(n)}(0)$, which leads to the explicit values,

$$\hat{I}_{qq}^{(-1)} = 0, \quad \hat{I}_{q1}^{(-1)} = \frac{-1+i}{\delta}, \quad \hat{I}_{q\zeta}^{(-1)} = 1, \quad (33)$$

$$\hat{I}_{qq}^{(0)} = 1, \quad \hat{I}_{q1}^{(0)} = 1, \quad \hat{I}_{q\zeta}^{(0)} = 0,$$

$$\hat{I}_{qq}^{(1)} = -\frac{1}{2}\delta, \quad \hat{I}_{q1}^{(1)} = -\frac{1+i}{2}\delta, \quad \hat{I}_{q\zeta}^{(1)} = -\frac{i}{2}\delta^2,$$

$$\hat{I}_{qq}^{(2)} = \frac{1}{4}\delta^2, \quad \hat{I}_{q1}^{(2)} = \frac{i}{2}\delta^2, \quad \hat{I}_{q\zeta}^{(2)} = -\frac{1-i}{2}\delta^3,$$

$$\hat{I}_{qq}^{(3)} = -\frac{1}{8}\delta^3, \quad \hat{I}_{q1}^{(3)} = \frac{1-i}{4}\delta^3, \quad \hat{I}_{q\zeta}^{(3)} = \frac{3}{4}\delta^4,$$

$$\hat{I}_{qq}^{(4)} = \frac{1}{16}\delta^4, \quad \hat{I}_{q1}^{(4)} = -\frac{1}{4}\delta^4, \quad \hat{I}_{q\zeta}^{(4)} = -\frac{1+i}{2}\delta^5.$$

We can now find the analytical solution for \mathbf{v}_2^δ to be used in the slip boundary condition (25d) for the bulk streaming velocity \mathbf{v}_2^{d0} at the wall $\zeta = 0$. As shown in Appendix B, \mathbf{v}_2^δ is found by integrating Eq. (28) twice

from $\zeta = \infty$, where it is zero, to ζ using that: (1) the right-hand-side of Eq. (28), called f^{rhs} , can be separated in the in-plane and perpendicular coordinates (ξ, η) and ζ , respectively, (2) f^{rhs} forms a linear superposition of functions $f_{\alpha}^{\text{rhs}}(\xi, \eta) I_{ab}^{(n_{\alpha})}(\zeta)$, $\alpha = 1, 2, \dots, M$, and (3) the functions $I_{ab}^{(n_{\alpha})}(\zeta)$ have the special properties summarized in Eq. (30), notably the integration property (30b) that changes a ζ -integration into a simple increase by unity of the index n_{α} . The structure of the computation of \mathbf{v}_2^{δ} is simply (see details in Appendix B),

$$\partial_{\zeta}^2 \mathbf{v}_2^{\delta} = \sum_{\alpha=1}^M f_{\alpha}^{\text{rhs}}(\xi, \eta) I_{ab}^{(n_{\alpha})}(\zeta), \quad \text{which implies} \quad (34a)$$

$$\mathbf{v}_2^{\delta} = \sum_{\alpha=1}^M f_{\alpha}^{\text{rhs}}(\xi, \eta) I_{ab}^{(n_{\alpha}+2)}(\zeta). \quad (34b)$$

The surface value $\mathbf{v}_2^{\delta 0}$ of the boundary-layer field \mathbf{v}_2^{δ} is derived in Appendix B in terms of its tangential and normal components, including the pre-factor $\frac{1}{v_0} = \frac{2}{\omega \delta^2}$ and by substituting the bulk factors $I_{ab}^{(n)}(\zeta)$ with their surface values $\hat{I}_{ab}^{(n)}$ given in Eq. (33), with $\frac{2}{\omega \delta^2} \hat{I}_{qq}^{(n)}$, $\frac{2}{\omega \delta^2} \hat{I}_{1q}^{(n)} \propto \delta^{n-2}$ and $\frac{2}{\omega \delta^2} \hat{I}_{\zeta q}^{(n)} \propto \delta^{n-1}$. The result is

$$\mathbf{v}_2^{\delta 0} = \mathbf{v}_{2\parallel}^{\delta 0} + v_{2\zeta}^{\delta 0} \mathbf{e}_{\zeta}, \quad (35a)$$

$$\mathbf{v}_{2\parallel}^{\delta 0} = \frac{2}{\omega \delta^2} \left\{ -\nabla_{\parallel} \left[\langle \hat{I}_{qq}^{(2)} v_{1\zeta}^{\delta 0}, v_{1\zeta}^{\delta 0} \rangle \right. \right. \\ \left. \left. + \langle \hat{I}_{1q}^{(2)} v_{1\zeta}^{d0}, v_{1\zeta}^{\delta 0} \rangle + \langle \hat{I}_{q1}^{(2)} v_{1\zeta}^{\delta 0}, v_{1\zeta}^{d0} \rangle \right] \right. \\ \left. + \nabla_{\parallel} \cdot \langle \hat{I}_{qq}^{(2)} \mathbf{v}_{1\parallel}^{\delta 0}, \mathbf{v}_{1\parallel}^{\delta 0} \rangle + \langle \hat{I}_{qq}^{(1)} \mathbf{v}_{1\parallel}^{\delta 0}, v_{1\zeta}^{\delta 0} \rangle \right. \\ \left. + \nabla_{\parallel} \cdot \langle \hat{I}_{1q}^{(2)} \mathbf{v}_{1\parallel}^{d0}, \mathbf{v}_{1\parallel}^{\delta 0} \rangle + \langle \hat{I}_{1q}^{(1)} \mathbf{v}_{1\parallel}^{d0}, v_{1\zeta}^{\delta 0} \rangle \right. \\ \left. + \nabla_{\parallel} \cdot \langle \hat{I}_{q1}^{(2)} \mathbf{v}_{1\parallel}^{\delta 0}, \mathbf{v}_{1\parallel}^{d0} \rangle + \langle \hat{I}_{q1}^{(1)} \mathbf{v}_{1\parallel}^{\delta 0}, v_{1\zeta}^{d0} \rangle \right. \\ \left. + \langle \hat{I}_{\zeta q}^{(1)} \partial_{\zeta} \mathbf{v}_{1\parallel}^{d0}, v_{1\zeta}^{\delta 0} \rangle + \langle \hat{I}_{q\zeta}^{(1)} \mathbf{v}_{1\parallel}^{\delta 0}, \partial_{\zeta} v_{1\zeta}^{d0} \rangle \right\}, \quad (35b)$$

$$v_{2\zeta}^{\delta 0} = -\frac{2}{\omega \delta^2} \left\{ \right. \\ \left. + \nabla_{\parallel} \cdot \left[\nabla_{\parallel} \cdot \langle \hat{I}_{qq}^{(3)} \mathbf{v}_{1\parallel}^{\delta 0}, \mathbf{v}_{1\parallel}^{\delta 0} \rangle + \langle \hat{I}_{qq}^{(2)} \mathbf{v}_{1\parallel}^{\delta 0}, v_{1\zeta}^{\delta 0} \rangle \right] \right. \\ \left. + \nabla_{\parallel} \cdot \left[\nabla_{\parallel} \cdot \langle \hat{I}_{1q}^{(3)} \mathbf{v}_{1\parallel}^{d0}, \mathbf{v}_{1\parallel}^{\delta 0} \rangle + \langle \hat{I}_{1q}^{(2)} \mathbf{v}_{1\parallel}^{d0}, v_{1\zeta}^{\delta 0} \rangle \right] \right. \\ \left. + \nabla_{\parallel} \cdot \left[\nabla_{\parallel} \cdot \langle \hat{I}_{q1}^{(3)} \mathbf{v}_{1\parallel}^{\delta 0}, \mathbf{v}_{1\parallel}^{d0} \rangle + \langle \hat{I}_{q1}^{(2)} \mathbf{v}_{1\parallel}^{\delta 0}, v_{1\zeta}^{d0} \rangle \right] \right. \\ \left. + \nabla_{\parallel} \cdot \left[\langle \hat{I}_{\zeta q}^{(2)} \partial_{\zeta} \mathbf{v}_{1\parallel}^{d0}, v_{1\zeta}^{\delta 0} \rangle + \langle \hat{I}_{q\zeta}^{(2)} \mathbf{v}_{1\parallel}^{\delta 0}, \partial_{\zeta} v_{1\zeta}^{d0} \rangle \right] \right\}. \quad (35c)$$

Here, terms to the two lowest powers in the small length scale δ are kept, which for Eq. (35b) is δ^{-1} and δ^0 , and for Eq. (35c) is δ^0 and δ^1 . These expressions for $\mathbf{v}_2^{\delta 0}$ are central in the BL25 model. In BL18 only the lowest power δ^{-1} in Eq. (35b) and δ^0 in Eq. (35c) was kept.

B. Long-range bulk streaming

The governing equations for the 2nd-order bulk streaming follow from the long-range part of Eq. (24),

and they are the same as in the BL18 model,

$$\rho_0 \nabla \cdot \mathbf{v}_2^d = \nabla \cdot \langle \rho_1 \mathbf{v}_1^d \rangle, \quad (36a)$$

$$\nabla \cdot \boldsymbol{\sigma}_2^d = \rho_0 \nabla \cdot \langle \mathbf{v}_1^d \mathbf{v}_1^d \rangle \\ = \rho_0 \langle \mathbf{v}_1^d \cdot \nabla \mathbf{v}_1^d \rangle + \rho_0 \langle \mathbf{v}_1^d \nabla \cdot \mathbf{v}_1^d \rangle, \quad (36b)$$

$$\text{with } \nabla \cdot \boldsymbol{\sigma}_2^d = -\nabla(p_2^d - \beta \eta_0 \nabla \cdot \mathbf{v}_2^d) + \eta_0 \nabla^2 \mathbf{v}_2^d. \quad (36c)$$

As shown in Ref. [31], the source terms in these equations can be evaluated using Eqs. (16) and (17),

$$\nabla \cdot \mathbf{v}_2^d = \Gamma \frac{k_0}{2c_0} |\mathbf{v}_1^d|^2 \approx 0, \quad (37a)$$

$$\eta_0 \nabla^2 \mathbf{v}_2^d = \nabla \tilde{p}_2^d - \frac{\Gamma \omega}{c_0^2} \langle p_1^d \mathbf{v}_1^d \rangle, \quad (37b)$$

$$\tilde{p}_2^d = p_2^d - \left(\frac{1}{4} \kappa_0 |\mathbf{p}_1^d|^2 - \frac{1}{4} \rho_0 |\mathbf{v}_1^d|^2 \right), \quad (37c)$$

where we have introduced the excess pressure \tilde{p}_2^d , which is the 2nd-order pressure p_2^d minus the time-averaged acoustic Lagrangian density.

Next, we express the 2nd-order boundary condition (25d), $\mathbf{v}_2^{d0} = -\mathbf{v}_2^{\delta 0} - \langle (\mathbf{s}_1 \cdot \nabla) \mathbf{v}_1 \rangle|_{\zeta=0}$ in terms of the 1st-order surface values \mathbf{V}_1^0 and \mathbf{v}_1^d of the wall velocity and the bulk acoustic velocity, respectively, noting that by Eq. (19b) we have $\mathbf{v}_1^{\delta 0} = \mathbf{V}_1^0 - \mathbf{v}_1^{d0}$. This has already been achieved for the surface value $\mathbf{v}_2^{\delta 0}$ of the boundary streaming in Eq. (35), only the Stokes-drift term $\mathbf{v}_2^{\text{sd}} = \langle (\mathbf{s}_1 \cdot \nabla) \mathbf{v}_1 \rangle|_{\zeta=0}$ needs to be treated here. We use Eq. (12) $\mathbf{s}_1 = \frac{i}{\omega} \mathbf{V}_1^0$, and Eqs. (14b) and (32) to compute in-plane and normal derivatives, and obtain

$$\mathbf{v}_2^{\text{sd}} = \langle (\mathbf{s}_1 \cdot \nabla) \mathbf{v}_1 \rangle|_{\zeta=0} \quad (38) \\ = \frac{1}{\omega} \left[\langle i(\mathbf{V}_1^0 \cdot \nabla), \mathbf{v}_1^d + \mathbf{v}_1^{\delta} \rangle \right]_{\zeta=0} \\ = \frac{1}{\omega} \left[\langle i\mathbf{V}_1^0 \cdot \nabla, \mathbf{v}_1^{d0} + \nabla_{\parallel} \mathbf{v}_1^{\delta 0} \rangle + \langle V_{1\zeta}^0, k_s \mathbf{v}_1^{\delta 0} \rangle \right].$$

The final form of the slip boundary condition (25d) for \mathbf{v}_2^{d0} , is obtained by combining Eqs. (35) and (38),

$$\mathbf{v}_2^{d0} = -(\mathbf{v}_2^{\delta 0} + \mathbf{v}_2^{\text{sd}}) = -(\mathbf{v}_{2\parallel}^{\delta 0} + \mathbf{v}_{2\parallel}^{\text{sd}}) - (v_{2\zeta}^{\delta 0} + v_{2\zeta}^{\text{sd}}) \mathbf{e}_{\zeta}. \quad (39)$$

In the BL25 model, the 2nd-order steady bulk streaming \mathbf{v}_2^d appears as a weakly compressible Stokes flow governed by Eq. (37), which is driven by the weak body force $-\frac{\Gamma \omega}{c_0^2} \langle p_1^d \mathbf{v}_1^d \rangle$ and by the slip-boundary condition (39). All the driving terms have the form of time-averaged products of the 1st-order fluid pressure and velocity fields p_1 and \mathbf{v}_1 and the 1st-order solid displacement field \mathbf{u}_1 with wall velocity \mathbf{V}_1^0 as described in Secs. II and III, respectively. In the following section we describe how this model is implemented in Comsol Multiphysics for numerical solution.

V. ACOUSTOFLUIDIC DEVICE MODELING

We introduce two polymer-based model systems, a 3D device driven by a thin-film transducer and a 2D device

TABLE I. The geometrical parameters for the 3D and 2D polymer-based devices considered here, see also Fig. 1.

Symbol	Value	Symbol	Value
<i>The 3D device driven by a $\text{Al}_{0.6}\text{Sc}_{0.4}\text{N}$ thin-film transducer</i>			
L_{sl}	500 μm	L_{fl}	300 μm
W_{sl}	475 μm	W_{fl}	275 μm
H_{sl}	320 μm	H_{fl}	120 μm
H_{pz}	2 μm	T_{wl}	100 μm
<i>The 2D device driven by a bulk PZT transducer</i>			
W_{sl}	2750 μm	W_{fl}	392 μm
H_{sl}	650 μm	H_{fl}	351 μm
W_{pz}	3500 μm	W_{gr}	150 μm
H_{pz}	500 μm	H_{gr}	100 μm
H_{el}	9 μm	H_{gl}	20 μm

driven by a bulk transducer, as sketched in Fig. 1 with the specific geometrical parameters listed in Table I. The top electrode of the transducer in both models are split by a groove to ensure an efficient excitation of a selected antisymmetric resonance mode.

A. The 3D model with a thin-film transducer

The 3D model is made as small as possible to allow for simulations using the Full model within the available 600-GB-RAM memory capacity of our computer system, while still containing all essential elements of an acoustofluidic device: a fluid cavity (fl) embedded in a solid (sl), which is driven by an attached piezoelectric transducer (pz). Spurious corner effects are avoided by choosing an ellipsoidal fluid domain with principal axes $L_{\text{fl}} \gtrsim W_{\text{fl}} \gtrsim H_{\text{fl}}$, all less than 300 μm . The dimensions of the box-shaped solid of length L_{sl} , width W_{sl} , and height H_{sl} are less than 500 μm , which results in resonance frequencies in the relevant 1-2 MHz range. The elastic solid is the polymer poly(methyl methacrylate) (PMMA), and the smallest possible transducer is a thin-film $\text{Al}_{0.6}\text{Sc}_{0.4}\text{N}$ transducer of height $H_{\text{pz}} \simeq 2 \mu\text{m}$, which covers the bottom surface of the solid as studied in Refs. [40, 41].

Finally, by assuming the yz - and xz -plane to be a symmetry and an anti-symmetry plane, respectively, the computational domain is reduced to a quarter of the full domain. The boundary conditions presented in the previous sections therefore needs to be supplemented by the following (anti-)symmetry-plane conditions valid for each perturbation order,

$$\text{Symmetry at } x = 0: \quad (40a)$$

$$\begin{aligned} \partial_x p_1 = 0, \quad \partial_x \varphi_1 = 0, \quad u_{1,x} = 0, \quad \sigma_{1yx}^{\text{sl}} = \sigma_{1zx}^{\text{sl}} = 0, \\ \partial_x p_2 = 0, \quad v_{2x}^d = 0, \quad \sigma_{2yx}^{d,\text{fl}} = \sigma_{2zx}^{d,\text{fl}} = 0, \end{aligned}$$

$$\text{Symmetry at } y = 0: \quad (40b)$$

$$\partial_y p_2 = 0, \quad v_{2y}^d = 0, \quad \sigma_{2xy}^{d,\text{fl}} = \sigma_{2zy}^{d,\text{fl}} = 0,$$

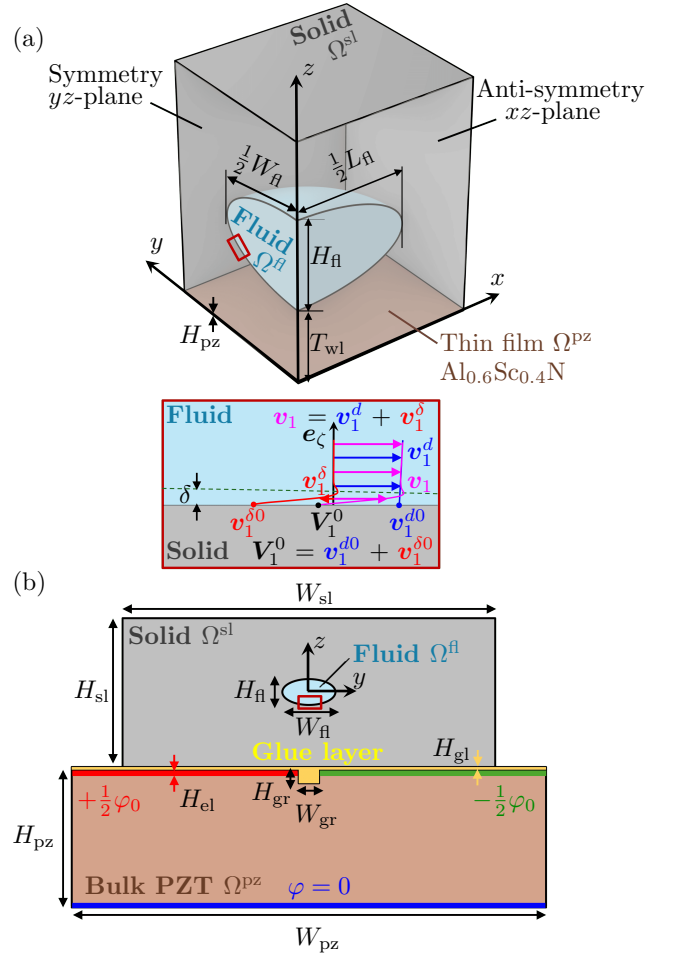


FIG. 1. Two acoustofluidic device models used for numerical validation of the BL25 model against the Full model, see parameter values in Table I. (a) The small sub-mm 3D model consisting of an ellipsoidal fluid domain embedded in a solid with a thin-film $\text{Al}_{0.6}\text{Sc}_{0.4}\text{N}$ transducer attached on its lower surface. (b) The 2D mm-sized model consisting of an elliptic fluid domain embedded in a solid, which is attached to a bulk PZT transducer via a glue layer. The inset is a zoom-in of the fluid-solid interface that illustrates the Helmholtz decomposition (16) $\mathbf{v}_1 = \mathbf{v}_1^d + \mathbf{v}_1^\delta$ of the acoustic velocity field.

$$\text{Anti-symmetry at } y = 0: \quad (40c)$$

$$p_1 = 0, \quad \varphi_1 = 0, \quad \sigma_{1yy}^{\text{sl}} = 0, \quad u_{1x} = u_{1z} = 0,$$

Finally, as there in the symmetry-reduced model are only a top and a bottom electrode on the transducer, the potential boundary condition (8a) becomes,

$$\varphi_1 = +\frac{1}{2}\varphi_0, \quad \text{for } \mathbf{r} \in \partial\Omega_{\text{top}}^{\text{pz}}, \quad (41a)$$

$$\varphi_1 = 0, \quad \text{for } \mathbf{r} \in \partial\Omega_{\text{bottom}}^{\text{pz}}, \quad (41b)$$

The 20-nm-thick metal electrodes are not explicitly included in the model, but they appear indirectly through the potential values (41) on the transducer surfaces.

B. The 2D model with a bulk transducer

The 2D model is nearly the same as the cross section of the actual mm-sized bulk-transducer-driven polymer-based device studied in Ref. [20]. However, to avoid spurious corner effects in the numerical validation, we have changed the original rectangular fluid domain to a smooth elliptical domain with major axis W_{fl} and minor axis H_{fl} . The rectangular solid and bulk lead-zirconate-titanate (PZT) transducer has width \times height given by $W_{\text{sl}} \times H_{\text{sl}}$ and $W_{\text{pz}} \times H_{\text{pz}}$, respectively. The glue layer between the transducer and the solid has the thickness H_{gl} , the thickness of the electrodes is H_{el} , and the glue-filled groove in the top electrode has width W_{gr} and height H_{gr} . Note that in this model there are three isotropic elastic solid domains with corresponding Cauchy momentum equations (4): the PMMA wall (sl = pm), the glue layer (sl = gl), and the silver electrodes (sl = el), and that the boundary conditions (6b) according to Fig. 1 instead of only $\partial\Omega_{\text{sl}}^{\text{PZ}}$ now include three types of interfaces $\partial\Omega_{\text{gl}}^{\text{PZ}}$, $\partial\Omega_{\text{el}}^{\text{PZ}}$, and $\partial\Omega_{\text{gl}}^{\text{pm}}$.

Finally, the potential boundary condition (8a) is specified by the anti-symmetric form around the $y = 0$ line of the voltages applied to each of the three electrodes of the 2D device, the top-left, top-right, and bottom electrode,

$$\varphi_1 = +\frac{1}{2}\varphi_0, \quad \text{for } \mathbf{r} \in \partial\Omega_{\text{top-left}}^{\text{PZ}}, \quad (42a)$$

$$\varphi_1 = -\frac{1}{2}\varphi_0, \quad \text{for } \mathbf{r} \in \partial\Omega_{\text{top-right}}^{\text{PZ}}, \quad (42b)$$

$$\varphi_1 = 0, \quad \text{for } \mathbf{r} \in \partial\Omega_{\text{bottom}}^{\text{PZ}}, \quad (42c)$$

VI. NUMERICAL IMPLEMENTATION IN COMSOL MULTIPHYSICS

Following the previous works from our group, the governing partial differential equations (PDE) are implemented in the finite-element method software COMSOL Multiphysics [42] using the “Weak Form PDE Interface” [31, 35] (see a sample script in the Supplemental Material of Ref. [43]). All simulations consist of two study steps: In step 1, the 1st-order acoustic equations are solved, and the result is passed on to step 2, in which the time-averaged 2nd-order equations are solved using the 1st-order solutions in the different source terms.

In the Full model, the acoustic fields are the pressure p_1 and the full acoustic velocity \mathbf{v}_1 in the fluid, the displacement \mathbf{u}_1 in the solids, and the electric potential φ_1 in the transducer. The governing equations of these fields are Eqs. (4), (7) and (15), and the corresponding boundary conditions are Eqs. (6), (8) and (42). The time-averaged fields are only the pressure p_2 and the full streaming field \mathbf{v}_2 in the fluid, with the governing Stokes-flow equation and Stokes-drift boundary condition both given in Eq. (24).

In the BL25 model, the acoustic field is just the pressure p_1 in the fluid, the displacement \mathbf{u}_1 in the solids, and the electric potential φ_1 in the transducer. The govern-

ing equations of these fields are Eqs. (4), (7) and (17c), and the corresponding boundary conditions are Eqs. (6) and (8) as well as the self-consistent, effective, boundary-layer conditions for the pressure and the stress, Eqs. (22) and (23). The time-averaged fields are only the excess pressure \tilde{p}_2^d and the long-range bulk streaming field \mathbf{v}_2^d in the fluid, with the governing weakly-compressional-Stokes-flow equation (37) and the effective boundary-layer velocity slip condition given by Eq. (39) in combination with Eqs. (35) and (38). An important technical note regards third derivatives in COMSOL, which appear several places in the boundary condition (35), such as $\partial_z \partial_y v_{1x}^d \propto \partial_z \partial_y \partial_x p_1$. In COMSOL, such a term is set to zero, as three consecutive derivatives of any field are not allowed. Consequently, we introduce an auxiliary vector field \mathbf{G}_1 equal to the pressure gradient ∇p_1 such that its k th component is $G_{1k} = \partial_k p_1$. Following Eq. (17a), we set $\mathbf{v}_1^d = -[i(1 - i\Gamma)/\omega\rho_0]\mathbf{G}_1$, which in COMSOL has nonzero second derivatives, such as $\partial_z \partial_y v_{1x}^d \neq 0$.

To understand the following details in the COMSOL implementation, it is relevant to mention that in COMSOL, the partial x -derivative $\partial_x f$ of a scalar field f is written by appending a lower-case “x” to “f” as “fx”. Thus the Cartesian coordinates of the gradient ∇f is written as “(fx,fy,fz)”. To avoid ambiguities, the Cartesian vector components of a vector \mathbf{v} are represented by upper-case letters such as “(vX,vY,vZ)”. The partial x -derivative $\partial_x v_x$ of the component v_x is thus written “vXx”.

In the COMSOL implementation of the effective boundary conditions of the BL25 model, the local tangential and normal unit vectors $\mathbf{e}_\xi = \mathbf{t}_1$, $\mathbf{e}_\eta = \mathbf{t}_2$, and $\mathbf{e}_\zeta = \mathbf{n}$, the tangential derivatives ∇_{\parallel} , and the time-average $\langle a_1, b_1 \rangle$ of 1st-order products $a_1 b_1$ play a crucial role. In COMSOL, the local tangential and normal vectors have the Cartesian components “(t1X,t1Y,t1Z)”, “(t2X,t2Y,t2Z)”, and “(nX,nY,nZ)”, respectively. As we work only in the limit of weakly-curved interfaces as described in Sec. IID, all ζ -derivatives of normal and tangential vectors are neglected. For example, the ζ -derivative $\partial_\zeta \mathbf{v}_\zeta$ of the of the ζ -component of the interface vector \mathbf{v}^0 is computed as $\partial_\zeta(\mathbf{n} \cdot \mathbf{v}^0) \approx \mathbf{n} \cdot \partial_\zeta \mathbf{v}^0 = n_i(n_k \partial_k) v_i^0$, which in COMSOL is the nine-term sum “nX*nX*vXx + nX*nY*vYx + ... + nZ*nZ*vZz”. The tangential derivatives are computed without approximations using the COMSOL operator “dtang()”, and the time averages are computed using the COMSOL operator “realdot()”. To avoid the spurious imaginary parts that sometimes appear, we explicitly take the real part, “real(realdot())” of all “realdot()” terms.

Since we cannot use δ as a superscript in COMSOL scripts, we introduce the superscript changes: $\delta \rightarrow$ “d” (for delta), $d \rightarrow$ “f” (for fluid bulk), and sl \rightarrow “s” (for solid). In COMSOL at the fluid-solid interface $\zeta = 0$, the Cartesian coordinates of the wall velocity \mathbf{V}_1^0 , the bulk fluid velocity \mathbf{v}_1^d , and the boundary-layer velocity \mathbf{v}_1^δ are written as “(vs1X,vs1Y,vs1Z)”, “(vf1X,vf1Y,vf1Z)”, and “(vd1X,vd1Y,vd1Z)”, where the latter according

to $\mathbf{v}_1^{d0} = \mathbf{V}_1^0 - \mathbf{v}_1^{d0}$ is computed as “(vs1X-vf1X, vs1Y-vf1Y, vs1Z-vf1Z)”. As mentioned above, \mathbf{G}_1 is introduced as an auxiliary field equal to ∇p_1 by the weak form definition “test(GK)*(GK-p1k)” for $K = X, Y, Z$ and $k = x, y, z$. The bulk velocity and its gradient are correspondingly defined as “vf1K = (1-i*Gam0)/(i*omega*rho0)*GK” and “vf1KN = (1-i*Gam0)/(i*omega*rho0)*GKn” with $K, N = X, Y, Z$ and $n = x, y, z$. All tangential derivatives after coordinate k of component K of the wall velocity \mathbf{V}_1^0 is computed as “vs1Ktk = dtang(vs1K,k)” with $K = X, Y, Z$ and $k = x, y, z$, and similar for \mathbf{v}_1^{d0} and \mathbf{v}_1^{d0} . Here, “Ktk” in the name “vs1Ktk” is read as “the K th component’s tangential k -derivative”.

Using this notation, we implement all the governing equations and boundary conditions of the BL25 model. In the following we show, how the 1st-order boundary conditions are implemented, and then refer to Appendix C for a more detailed description including the elaborate 2nd-order boundary conditions. The 1st-order pressure boundary condition (22) is written as “i*omega*rho0/(1-i*Gam0)*(nX*vs1X+nY*vs1Y + nZ*vs1Z - ii/ks*divparvs10) - ii/ks * (kc^2*p1 + p1zetazeta)”, where “divparvs10” is the tangential divergence $\nabla_{\parallel} \cdot \mathbf{V}_1^0$ written as “vs1XtX+vs1YtY+vs1ZtZ” and “p1zetazeta” is the 2nd-order ζ -derivative $\partial_{\zeta}^2 p_1 = (\mathbf{n} \cdot \nabla)(\mathbf{n} \cdot \nabla)p_1$ written as “= nX*nX*p1xx + 2*nX*nY*p1xy + 2*nX*nZ*p1xz + nY*nY*p1yy + 2*nY*nZ*p1yz + nZ*nZ*p1zz”. Similarly, the k -component $e_k \cdot \sigma_1^{sl} \cdot e_c$ of the 1st-order stress boundary condition (23) is written as “-p1*nK + i*ks*eta0 *(vd1K+nK*vd1zeta)”, where $K = X, Y, Z$ and “vd1zeta = vd1X*nX+vd1Y*nY+vd1Z*nZ”.

VII. NUMERICAL VALIDATION

To validate the BL25 model numerically, we have simulated the 3D and 2D polymer-based acoustofluidic devices with elliptical fluid channels shown in Fig. 1 and with the material parameters tabulated in Table II. As described below, the BL25-model results were successfully first tested for internal consistency by performing a mesh-convergence test, and then they were compared with results obtained by direct numerical simulations of the same devices using the Full model. In 3D, we find that using the Full-model for direct numerical simulation of acoustofluidic devices of typical experiments [10, 44] is out of the question, as it would required more than 1,000 GB of memory making it harder to simulate even using the DTU High Performance Computing (HPC) cluster at our disposal. Hence, we consider the tiny, yet physically realistic, device described above, which, although not of practical use, at least allows us to compare the BL25 model solutions with the Full model solutions. We remark that even with this tiny device, we are close to the limit of the finest mesh resolution that we can obtain when running the Full model on the DTU

HPC cluster. In the 2D case, we are not near this mesh resolution limit, and we compared both the BL25 and the BL18 model to the Full model.

Qualitative validation in the form of plots, are for selected field components g supplemented by the quantitative relative deviation $\epsilon_2(g^B, g^F)$ of the BL-model field g^B from the Full model field g^F using the L^2 -norm on the domain Ω [22],

$$\epsilon_2(g^B, g^F) = \frac{\|g^B - g^F\|_2}{\|g^F\|_2}, \text{ with } \|g\|_2 = \sqrt{\int_{\Omega} |g|^2 dV}. \quad (43)$$

A short summary of the following validation results is, that the BL25 model can predict the Full model results accurately for 1st- and 2nd-order fields in 3D and 2D, on and off resonance, and for hard glass-silicon and soft polymer devices. In contrast, the BL18 model (only tested in 2D) proved accurate only for 1st- and 2nd-order fields in hard glass-silicon devices run on resonance.

A. Mesh convergence and computational times in 2D and 3D of the BL25 and Full model

We have performed a mesh-convergence study for both the 3D and 2D model to determine the mesh, which gives a sufficient resolution for finding correctly converged solutions, see the details in Appendix D. The mesh size is quantified by a mesh scale s with $0.05 < s < 0.85$. When s is increased more and smaller mesh elements are introduced, and a better resolved mesh results. For a given field component g , we make a semi-log plot $\epsilon_2(g_s, g_{0.85})$ versus s of the relative deviation $\epsilon_2(g_s, g_{0.85})$ of the solution g_s with mesh scale s from the solution $g_{0.85}$ with the maximum mesh scale $s = 0.85$ (the finest mesh). For all fields (in 1st order $p_1, v_{1,i}$ with $i = x, y, z$), $u_{1,i}$ with $i = x, y, z$), and φ_1 , and in 2nd order $p_2, v_{2,i}$ with $i = x, y, z$), we find that $\epsilon_2(s)$ for $s \gtrsim 0.2$ is well described by an exponential decay, which indicates that convergence is obtained. In particular for $s = 0.7$, all relative deviations are small, $\epsilon_2(0.7) < 0.01$, and we therefore choose this value of s as our converged mesh. As in Ref. [22], the 1st-order fields converge faster than the 2nd-order fields.

The computational time and memory requirement for the various simulations using the converged mesh scale $s = 0.7$ are as follows. In 2D, all simulations are done using COMSOL 6.2 on a HP-Z4 workstation with a processor Intel(R) Xeon(R) W-2295 CPU @3.00 GHz and 512 GB of random access memory (RAM). All 2D simulations uses the same 2D mesh, which has 23,145 mesh elements with 12,712 mesh vertices, which for the Full model results in 543,107 degrees of freedom (DoF), a computational time of 48 s, and a memory usage of 16.8 GB RAM, and which for the BL25 model results in 363,915 DoF, a computational time of 30 s, and a memory usage of 14.8 GB RAM.

TABLE II. Parameters values at 25 °C used in the numerical simulation of fluids (water, iodixanol-water, glycerol-water), solids (PMMA, NOA86H glue), and transducers (PZT Pz27 and $\text{Al}_{0.6}\text{Sc}_{0.4}\text{N}$). For the isotropic solids $C_{12} = C_{11} - 2C_{44}$, and for the transducers $C_{12} = C_{11} - 2C_{66}$.

Parameter	Symbol	Value	Unit
<i>Water</i> [24]			
Mass density	ρ^{fl}	997.05	kg m^{-3}
Speed of sound	c_{fl}	1496.7	m s^{-1}
Compressibility	κ_{fl}	447.7	TPa^{-1}
Dynamic viscosity	η_{fl}	0.89	mPa s
Bulk viscosity	$\eta_{\text{fl}}^{\text{b}}$	2.485	mPa s
<i>Iodixanol-water 16 % V/V solution</i> [20, 24]			
Mass density	ρ^{fl}	1050.0	kg m^{-3}
Speed of sound	c_{fl}	1482.3	m s^{-1}
Compressibility	κ_{fl}	433.4	TPa^{-1}
Dynamic viscosity	η_{fl}	1.474	mPa s
Bulk viscosity	$\eta_{\text{fl}}^{\text{b}}$	1.966	mPa s
<i>Glycerol-water 99 % V/V solution</i> [20, 45]			
Mass density	ρ^{fl}	1260.4	kg m^{-3}
Speed of sound	c_{fl}	1922.8	m s^{-1}
Compressibility	κ_{fl}	214.6	TPa^{-1}
Dynamic viscosity	η_{fl}	1.137	Pa s
Bulk viscosity	$\eta_{\text{fl}}^{\text{b}}$	0.790	Pa s
<i>PMMA</i> [39]			
Mass density	ρ^{sl}	1162	kg m^{-3}
Elastic modulus	C_{11}	7.18 – i0.183	GPa
Elastic modulus	C_{44}	1.55 – i0.111	GPa
<i>Glue layer (NOA 86H)</i> [39]			
Mass density	ρ^{sl}	1300	kg m^{-3}
Elastic modulus	C_{11}	4.65 – i0.51	GPa
Elastic modulus	C_{44}	1.21 – i0.12	GPa
<i>PZT Pz27 bulk transducer</i> [46]			
Mass density	ρ^{pz}	7700	kg m^{-3}
Elastic modulus	C_{11}	124 – i0.601	GPa
Elastic modulus	C_{12}	77 – i0.442	GPa
Elastic modulus	C_{13}	80 – i0.091	GPa
Elastic modulus	C_{33}	119 – i0.538	GPa
Elastic modulus	C_{44}	20.4 – i0.486	GPa
Coupling constant	e_{15}	11.0	C m^{-2}
Coupling constant	e_{31}	–5.2	C m^{-2}
Coupling constant	e_{33}	16.3	C m^{-2}
Electric permittivity	ε_{11}	982 ε_0	F m^{-1}
Electric permittivity	ε_{33}	804(1 – i0.003) ε_0	F m^{-1}
<i>$\text{Al}_{0.6}\text{Sc}_{0.4}\text{N}$ thin-film transducer</i> [41, 47, 48]			
Mass density	ρ^{pz}	3300	kg m^{-3}
Elastic modulus	C_{11}	313.8 – i0.157	GPa
Elastic modulus	C_{12}	150 – i0.075	GPa
Elastic modulus	C_{13}	139.2 – i0.069	GPa
Elastic modulus	C_{33}	197.1 – i0.099	GPa
Elastic modulus	C_{44}	108.6 – i0.054	GPa
Coupling constant	e_{15}	–0.317	C m^{-2}
Coupling constant	e_{31}	–2.653	C m^{-2}
Coupling constant	e_{33}	2.734	C m^{-2}
Electric permittivity	ε_{11}	22.5(1 + i0.0005) ε_0	F m^{-1}
Electric permittivity	ε_{33}	22.5(1 + i0.0005) ε_0	F m^{-1}

For the 3D simulations, despite the small-sized device geometry, the computational time and memory requirement of the Full model forced us to use the DTU HPC

cluster. To obtain a fair comparison of the computational time requirement between the Full model and the BL25 model, we therefore also ran the latter on the DTU HPC cluster. In 3D, the Full model mesh has 101,839 mesh elements with 25,060 vertices, which results in 2,536,778 DoF, a computational time of 26 min 26 s, and a memory usage of 348 GB RAM. In contrast, the 3D mesh of the BL25 model has only 35,098 mesh elements with 6,344 vertices, which results in 278,078 DoF, a computational time of 1 min 11 s, and a memory usage of 33 GB RAM. Here we clearly see the huge reduction in the computational requirements, when going from the Full model to the BL25 model in 3D simulations. We end by noting that the much higher computational cost of the Full model is caused not only by the fine resolution needed in the thin boundary layer, which by construction is avoided in the BL25 model, but also because to obtain the same accuracy, the Full model requires a finer mesh in the bulk than the BL25 model.

B. 3D numerical validation of BL25 vs. Full model: the tiny PMMA device with an ellipsoidal cavity

We now turn to the numerical validation of the BL25 model by comparing it to the Full model. This is done on the tiny sub-mm PMMA-based ellipsoidal-cavity device actuated by a thin-film transducer described in Sec. V A. The comparison covers simulation of the 1st- and 2nd-order fields mentioned in Sec. VII, and we remark that to the best of our knowledge, the Full model simulations are the first of its kind carried out for a 3D acoustofluidic device.

The thin-film transducer is attached at the bottom of the device as shown in Fig. 1(a), and the device is actuated by applying an AC voltage with frequency f and amplitude $+\frac{1}{2}\varphi_0$ ($-\frac{1}{2}\varphi_0$) on the top left-half (right-half) of the split top electrode, $\varphi_0 = 1$ V, and by grounding the bottom electrode. Using the BL25 model, the resonance frequency for the PMMA device is obtained as the position $f_{\text{res}} = 2.03$ MHz of the maximum energy density $E_{\text{ac}}(f)$ in a frequency sweep from 0 to 2.5 MHz in steps of 5.0 kHz, and we find that $E_{\text{ac}}(f_{\text{res}}) = 0.06 \text{ J m}^{-3}$. Then we compute the 1st- and 2nd-order acoustic fields in both the BL25 and the Full model at f_{res} . The comparison of 1st- and 2nd-order fields in the two models are presented in Fig. 2(a1) and Fig. 2(b1), respectively. The relative deviation between the models are $\varepsilon_2^{\text{1st}} \lesssim 0.5\%$ and $\varepsilon_2^{\text{2nd}} \lesssim 2\%$ for the 1st- and 2nd-order fields, respectively, and both models find that for example that the 1st-order acoustic pressure inside the fluid channel has the amplitude 21 kPa and that the maximum solid displacement of the PMMA is 1.5 nm. The 2nd-order velocity (streaming) fields are notoriously difficult to compute. We obtained it in the BL25 model by computing \mathbf{v}_2^d using Eq. (36) along with the slip boundary conditions (39), and in the Full model we solved the 2nd-order Eq. (24) to obtain the streaming fields also inside the nu-

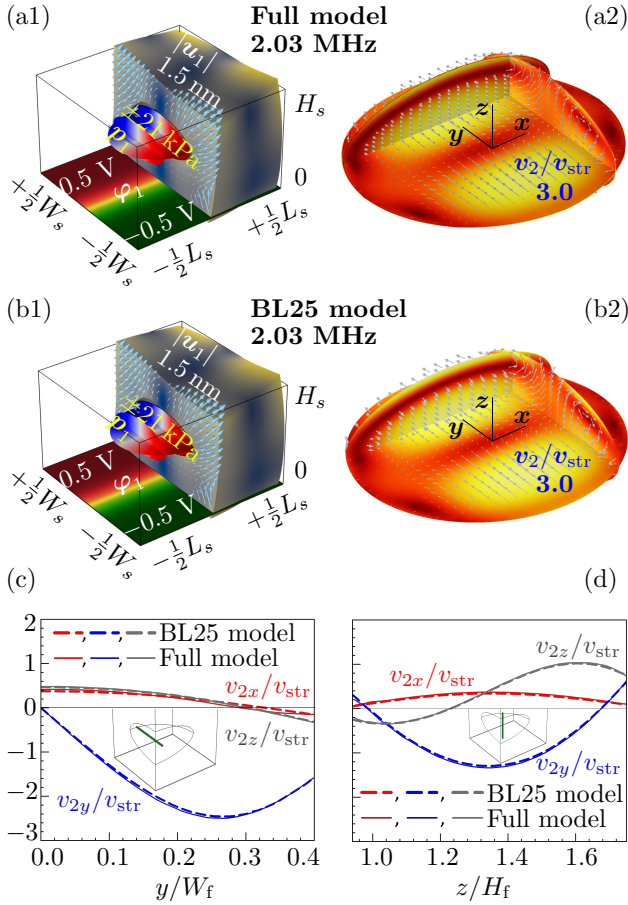


FIG. 2. Validating the 1st- and 2nd-order fields of the BL25 model against the Full model for the tiny sub-mm 3D PMMA device actuated by a piezoelectric split-top-electrode thin-film transducer at the resonance frequency $f_{\text{res}} = 2.03$ MHz, see Fig. 1(a) and Table I. (a1) Color plot of the Full model 1st-order pressure p_1 from -21 kPa (blue) to $+21$ kPa (red), the amplitude of the displacement field, $|\mathbf{u}_1|$ from 0 (dark blue) to 1.5 nm (yellow), and the electrical potential φ_1 from -0.5 V (green) to $+0.5$ V (red). (a2) Vector plot of the Full model streaming velocity \mathbf{v}_2 and color plot of its normalized magnitude v_2/v_{str} from 0 (Dark brown) to 3.0. (b1) Same as (a1), but for the BL25 model. (b2) Same as (a2), but for the BL25 model. (c) Line plots of the streaming field components comparison for the Full and BL25 models along the green line parallel to the y -direction. (d) Same as (c), but plotting along the green line parallel to the z -axis.

merically resolved boundary layers. The contour plots of the streaming velocity \mathbf{v}_2 for the 3D tiny PMMA device obtained in the two models are shown in Fig. 2(a2) and Fig. 2(b2), respectively. We obtained the same streaming pattern in the two models in the bulk of the fluid volume, including the conventional Rayleigh streaming pattern with the four streaming rolls in the yz -plane, as well as the streaming pattern in the central xy -plane and xz -plane. In the plots we have normalized the streaming fields by the amplitude $v_{\text{str}} = \frac{3}{8} \frac{v_1^2}{c_0} = 0.06 \mu\text{m s}^{-1}$ of the conventional Rayleigh streaming.

The good agreement between the BL25 and Full model is further corroborated by plotting the respective streaming velocity components along the two lines passing through the point $(0.1L_f, 0.1W_f, 0.5H_f)$ parallel to the y - and z -axis respectively. The resulting line graphs are plotted in Fig. 2(c,d), where minor deviations can be seen closer to the boundary layers, which can be attributed to the coarser mesh used in the Full model. Since we are at the limit of the computational capability for using the Full model, the boundary layer in this model was not fully resolved, but nevertheless, the relative deviation in terms of L^2 -norms for the line plots were $\epsilon_2 \leq 1.7\%$.

C. 2D numerical validation of BL25 vs. Full model: normal-sized PMMA device with an elliptic cavity

As the final part of the numerical validation of the BL25 model, we consider the 2D cross-section of the normal-sized long, straight PMMA device with an elliptic water-filled microchannel, which was introduced in Fig. 1(b) together with the parameter lists in Tables I and II. Like conventional acoustofluidic devices, the 2D PMMA device is actuated by a bulk-sized piezoelectric transducer (PZT) glued by a thin layer of glue to the bottom surface of the PMMA block. Going to 2D has the advantage that the problems related to the extensive computer memory requirements in 3D are avoided, and we can also redo the numerical validation of the BL18 model, which was done only in 2D in the original work [31]. For better comparison, we have used the same mesh in Full and BL models in the present analysis, although a coarser mesh would suffice for the BL models [31].

Similar to the 3D device, the transducer of the 2D has a split top electrode, and it is actuated by applying an AC voltage with frequency f and amplitude $+\frac{1}{2}\varphi_0$ ($-\frac{1}{2}\varphi_0$) on the top left-half (right-half) of the split top electrode, $\varphi_0 = 1$ V, and by grounding the bottom electrode. As in 3D, the resonance frequencies f_{res} of the 2D PMMA device are obtained as the those leading to local maxima $E_{\text{ac}}(f_{\text{res}})$ when computing the acoustic energy density E_{ac} versus frequency from 0.5 MHz to 2.5 MHz in steps of 5 kHz. The relevant resonance frequency here is $f_{\text{res}} = 0.98$ MHz, which clearly, and in accordance with the WSUR principle for acoustically soft (PMMA) devices [21], is much lower than the corresponding resonance mode (~ 2 MHz) in an acoustically hard (glass) device.

In Fig. 3(a1,b1,c1) are shown the simulated contour plots of the 1st-order fields for the 2D PMMA device at resonance, $f_{\text{res}} = 0.98$ MHz, obtained from the Full model, the BL25 model, and the BL18 model, respectively. The resonance mode here, is a mixed-mode type with two pressure nodal lines (planes in 3D) parallel to y and z direction. The amplitude of the 1st-order acoustic pressure p_1 inside the channel is found to be 12.4 kPa, and the maximum displacement u_1 of the PMMA is 12.7 nm. All three models predict the same 1st-order

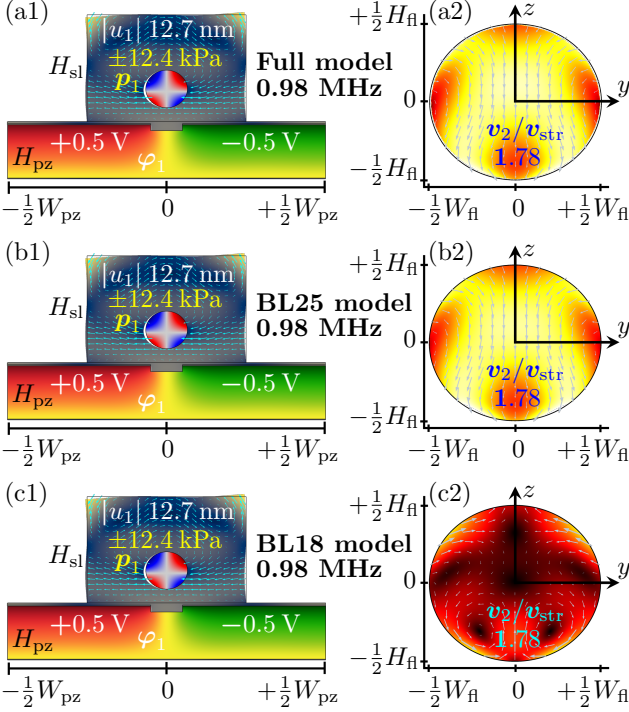


FIG. 3. Validating the 1st- and 2nd-order fields in the BL25 and BL18 model against the Full model for the mm-sized 2D PMMA device actuated by a piezoelectric split-top-electrode bulk transducer at the resonance frequency $f_{\text{res}} = 0.98$ MHz, see Fig. 1(b) and Table I. (a1) Full model 1st-order fields: pressure field, p_1 from -12.4 kPa (blue) to $+12.4$ kPa (red), the magnitude of solid displacement field $|u_1|$ from 0 (Dark blue) to 12.4 nm (yellow), the 1st-order electrical potential from -0.5 V (green) to $+0.5$ V (red) via the grounded electrode value of 0 V (yellow). (a2) Full model 2nd-order streaming field normalized with the Rayleigh streaming velocity from 0 (Dark red) to 1.78 (yellow). (b1) Similar to (a1), but for the BL25 model. (b2) Similar to (a2), but but for the BL25 model. (c1) Similar to (a1), but for the BL18 model. (c2) Similar to (a2), but for the BL18 model.

fields, and the relative deviations from the Full model is small, $\epsilon_2^{\text{1st}} \lesssim 0.01$ for both the BL25 and the BL18 model.

In Fig. 3(a2,b2,c2) are shown the simulated contour plots of the 2nd-order streaming field for the 2D PMMA device at resonance, $f_{\text{res}} = 0.98$ MHz, obtained from the Full model, the BL25 model, and the BL18 model, respectively. Whereas the BL25 model still has a small relative deviation from the Full model, $\epsilon_2(v_2^{\text{BL25}}, v_2^{\text{FM}}) = 2\%$, the BL18 model fails completely both quantitatively with $\epsilon_2(v_2^{\text{BL18}}, v_2^{\text{FM}}) = 96\%$ and predicting a qualitatively wrong solution. We note that when computing the L^2 -norm we exclude the region closer than $15 \mu\text{m}$ to avoid the boundary layers where the BL-models by construction deviate from the Full model. In this mixed-mode resonance, the conventional Rayleigh streaming pattern with four flow rolls does not appear, but for convenience we still plot the streaming fields normalized with the

TABLE III. The relative deviation $\epsilon_2(v_2^{\text{B}}, v_2^{\text{F}})$ of the BL25 and BL18 models from the Full model simulation of the acoustic streaming v_2 for elliptic channels with eccentricity $e = 0.44$ [Fig. 1(b)] and $e = 0.87$, embedded in (soft) PMMA and in (hard) glass, and actuated at the frequency f . Boldfaced entries are computed at resonance.

f (MHz)	2D device with PMMA		2D device with glass	
	$\epsilon_2(v_2^{\text{25}}, v_2^{\text{F}})$	$\epsilon_2(v_2^{\text{18}}, v_2^{\text{F}})$	$\epsilon_2(v_2^{\text{25}}, v_2^{\text{F}})$	$\epsilon_2(v_2^{\text{18}}, v_2^{\text{F}})$
<i>Elliptical channel cross section with eccentricity $e = 0.44$</i>				
0.98	4 %	96 %	3 %	16 %
1.52	2 %	13 %	1 %	27 %
3.66	3 %	24 %	1 %	7 %
4.02	1 %	14 %	1 %	9 %
<i>Elliptical channel cross section with eccentricity $e = 0.87$</i>				
0.98	3 %	148 %	3 %	20 %
1.97	1 %	25 %	1 %	2 %
3.95	1 %	13 %	2 %	36 %
4.27	1 %	18 %	2 %	16 %

Rayleigh streaming velocity $v_{\text{str}} = \frac{3}{8} \frac{v_1^2}{c_0} = 0.06 \mu\text{m s}^{-1}$. This comparison highlights the necessity of replacing the BL18 model by the BL25 model.

To further study the extend to which the BL25 and BL18 reproduce the Full model results for the 2nd-order streaming velocity, we supplement the current elliptical channel cross section with eccentricity 0.44 by another with eccentricity 0.87, both embedded in PMMA (soft) and in glass (hard). The respective relative deviations ϵ_2 from the Full model are listed in Table III.

Clearly, the BL25 model is more accurate than the BL18 model. The relative deviation of the BL25 model from the Full model is at most 4 %, whereas the BL18 model deviates typically 10 % or more. However, we note that the BL18 model is performing better for the hard glass devices than the soft PMMA devices, and the best performance of the BL18 model is at resonance frequencies in hard devices, exactly the case that have been tested previously [31, 35]. The reason for this behavior is that the pre-factors of the terms in the higher orders of $k\delta$ previously neglected, are so large that these term cannot be neglected. The inclusion of these term is exactly what distinguishes the BL25 model from the BL18 model, and we now see the result: The BL25 model is accurate both on and off resonance for both hard and soft devices. It is worth mentioning that the computation time of the complex and more accurate BL25 model is not significantly different from the more simple BL18 model. The reason is that the model complexity only affects the short time for initializing the finite-element matrix, but not the subsequent long time spend by the finite-element solver.

So far, we have only discussed geometries without sharp corners. However, the right angles in a rectangular channel cross section are sharp with a zero curvature. Thus, this common geometry breaks the fundamental assumption of weak curvature, on which the boundary-

TABLE IV. The geometry parameters (Parm.) and their values for the PMMA-based acoustofluidic device of Ref [20] used in the present BL25-model simulation of the device.

Parm.	Value	Parm.	Value	Parm.	Value
L_{pz}	24 mm	W_{pz}	8 mm	H_{pz}	2 mm
L_{sl}	50 mm	W_{sl}	5 mm	H_{sl}	1.18 mm
		H_{gl}	100 μm	H_{sl}^{lid}	0.18 mm
L_{gr}	24 mm	W_{gr}	300 μm	H_{gr}	65 μm
L_{fl}	40 mm	W_{fl}	375 μm	H_{fl}	150 μm

layer models are founded. To investigate corner effects, we have simulated 2D rectangular devices, and the results are presented in the Supplementary Material [37]. In summary, we found that in (hard) glass devices on resonance, the relative deviations are small for both BL25 and BL18, $\epsilon_2(v_2^{25}, v_2^F) = 0.4\%$ and $\epsilon_2(v_2^{18}, v_2^F) = 2\%$, but for the (soft) PMMA device, only BL25 remains accurate whereas BL18 fails, $\epsilon_2(v_2^{25}, v_2^F) = 4\%$ and $\epsilon_2(v_2^{18}, v_2^F) = 78\%$. So, also regarding corner effects in rectangular channels, the replacement of the BL18 model by the BL25 model is necessary for accurate simulations.

VIII. MODEL COMPARISON WITH EXPERIMENTAL DATA

Lastly, for an experimental validation of the BL25 model, we revisit the PMMA device (see Fig. 4(a)) fabricated and tested by Lickert *et al.* [20] to demonstrate by experiments and by numerical BL18-simulations that (soft) polymer-based acoustofluidic devices can perform acoustophoretic particle focusing. We show below that using the BL25 model together with updated values of the acoustic parameters of PMMA, we are able to predict quantitatively the measured resonance frequency f_{res} within 1 %, and both the electrical admittance Y and the acoustic energy density E_{ac} within 15 %. These results are an improvement of the BL18-model simulations of Ref. [20], which only predicted the measured f_{res} with quantitative accuracy, while Y and E_{ac} were predicted merely qualitatively.

The current experimental validation of the BL25 model was carried out in a seven-step procedure: (1) The acoustic parameters of the PMMA and the PZT transducer model Pz26 from CTS Ferroperm [49] were determined using our in-house ultrasound electrical induced spectroscopy (UEIS) method [39]. This contrasts the use of average literature values used in Ref. [20]. (2) The fluid properties for the iodixanol-water 16 % V/V and glycerol-water 99 % V/V solutions are set to the table values also used by Lickert *et al.* [20]. (3) The ill-determined thickness of the 'glue' layer (here, the 'glue' is actually the very viscous glycerol-water solution, but for simplicity still called 'glue') was initially set to 20 μm as in Ref. [20]. (4) The BL25 model was implemented in the water-filled channel where $\delta \approx 0.5\ \mu\text{m}$, whereas the

Full model was implemented in the highly viscous glycerol 'glue' layer, where $\delta \approx 20\ \mu\text{m}$ is so large that resolving the boundary layer numerically is unproblematic. (5) The simulation was then executed. The solid and fluid domain was discretized with tetrahedral mesh elements of maximum size, $h_{solid}^{max} = 375\ \mu\text{m}$ and $h_{fluid}^{max} = 93.75\ \mu\text{m}$, respectively, resulting in a mesh with 88,313 mesh elements, 13,670 boundary elements, and 1,711 edge elements, and the total DoF being 1,546,206. (6) We found that the glue-layer thickness plays a crucial role in damping the acoustic energy density in the fluid channel. Glycerol was used in the experiment to allow for easy mounting and dismounting of the device, but uniformity of the 'glue' layer thickness is difficult to control experimentally. Its thickness was not measured in the experiment, but merely assumed to lie in the range from 20 to 100 μm . A study of the effects of the glue-layer thickness on the acoustic energy density of the fluid is presented in the Supplemental Material [37]. There we conclude that a thickness of $H_{gl} = 100\ \mu\text{m}$ best fitted the experimental value of Y . (7) With $H_{gl} = 100\ \mu\text{m}$, we ran the BL25-model as a function of frequency from 0.5 to 2.5 MHz the same range as in Ref. [20].

The simulation results are shown in Fig. 4 including the 1st-order fields (pressure p_1 , displacement \mathbf{u}_1 , and electric potential φ_1), the acoustic radiation force Eq. (18b) \mathbf{F}^{rad} , and notably, the averaged acoustic energy density Eq. (18a) E_{ac} in the fluid, and the electrical admittance spectrum $Y(f)$ of the transducer loaded with PMMA and the fluid channel. Y is computed as the current I flowing into the positive electrode surface Ω_+ over the voltage difference φ_0 between the positive and the negative electrode, which in terms of D_z of Eq. (A2) is,

$$Y(f) = \frac{1}{\varphi_0} \int_{\Omega_+} \mathbf{J} \cdot (-\mathbf{n}) da = \frac{i\omega}{\varphi_0} \int_{\Omega_+} D_z da. \quad (44)$$

The electrical admittance spectrum is presented in Fig. 4(d). In the BL25-model simulation, the maximum admittance value $Y_{max}^{sim} = 4.4\ \text{mS}$ is obtained at the frequency $f_{res}^{sim} = 1.15\ \text{MHz}$, which defines the resonance frequency. This is in fair agreement with the measured values $Y_{max}^{exp} = 6.0\ \text{mS}$ obtained at $f_{res}^{exp} = 1.13\ \text{MHz}$. Also off-resonance in the entire frequency range, the BL25-model predicts fairly well within 10 - 30 % the entire admittance spectrum.

These results are consistent with the acoustic energy spectrum, presented in Fig. 4(e), where in the BL25 model, the simulated maximum energy value $E_{ac,max}^{sim} = 15\ \text{J m}^{-3}$ is obtained at $f_{res}^{sim} = 1.15\ \text{MHz}$, the same frequency as for Y_{max}^{sim} , and the measured maximum energy value $E_{ac,max}^{exp} = 13\ \text{J m}^{-3}$ is obtained at $f_{res}^{sim} = 1.13\ \text{MHz}$, the same frequency as for Y_{max}^{sim} . Thus $E_{ac,max}^{sim}$ deviates only 15 % from $E_{ac,max}^{exp}$, which an improvement of the numerical model compared to the 550 % deviation found in Ref. [20]. In short, we find that the BL25 model is validated against experimental data from the literature. The predicted resonance frequency deviates only 1 % from the

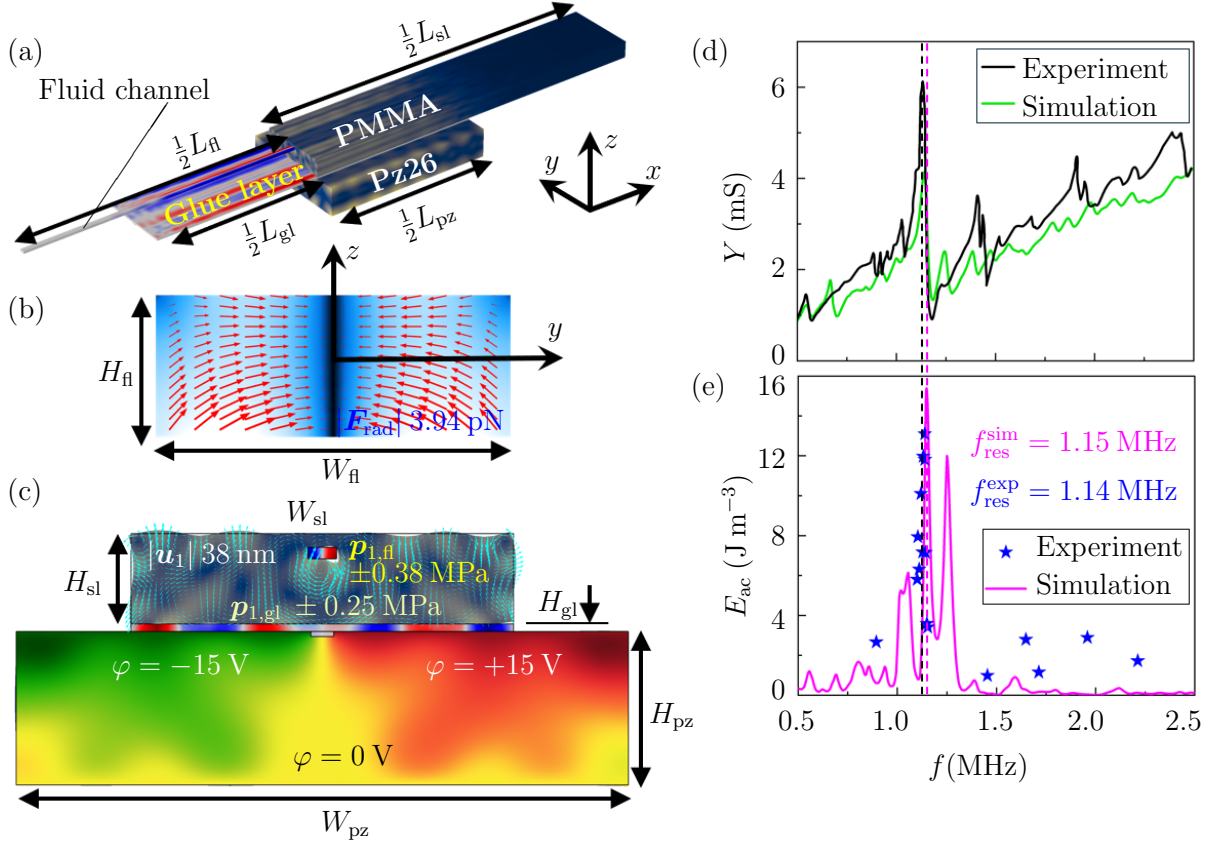


FIG. 4. BL25-model simulations in 3D of the PMMA device studied by Lickert *et al.* [20] with the parameters listed in Tables II, IV, and V. (a) Simulated 1st-order fields in 3D at the resonance frequency $f_{\text{res}} = 1.15$ MHz: the pressure inside the fluid channel [$p_{1,\text{fl}}$ from -0.38 MPa (blue) to $+0.38$ MPa (red)] and inside the glue layer [$p_{1,\text{gl}}$ from -0.25 MPa (blue) to $+0.25$ MPa (red)]. (b) A vector plot (red) of the simulated acoustic radiation force \mathbf{F}^{rad} and a color plot of its magnitude $|\mathbf{F}^{\text{rad}}|$ from 0 (black) to 3.94 pN (white) in the yz plane at $x = 0$. (c) Color and vector plots of the simulated 1st-order fields p_1 (both channel and coupling layer), \mathbf{u}_1 , and φ_1 in the cross-section in the yz -plane at $x = 0$. (d) The measured (black) and the simulated (green) electrical admittance Y plotted versus frequency f exhibiting a strong resonance near $f = 1.15$ MHz. (e) Measured (crosses) and simulated (line) acoustic energy density E_{ac} plotted versus frequency f . The measured and simulated resonance frequency f_{res} and corresponding $E_{\text{ac}}(f_{\text{res}})$ are found to be $f_{\text{res}}^{\text{exp}} = 1.14$ MHz with $E_{\text{ac}}^{\text{exp}} = 13 \text{ J m}^{-3}$ and $f_{\text{res}}^{\text{sim}} = 1.15$ MHz with $E_{\text{ac}}^{\text{sim}} = 15 \text{ J m}^{-3}$, respectively

measured one, and the predicted admittance and acoustic energy density deviates around 15 %.

We end this section by noting that we have observed that in the BL25 model the above fluid resonance frequency does not deviate from the resonance frequency of the unloaded Pz26 transducer, which in simulation and experiment was found to be $f_{\text{res}}^{\text{pz,sim}} = 1.145$ MHz and $f_{\text{res}}^{\text{pz,exp}} = 1.14$ MHz, respectively, in contrast to the mismatch between the resonance frequency of the unloaded transducer and the fluid reported by Lickert *et al.* [20].

The BL25 model corroborates the ability of the soft PMMA device to perform particle focussing. In Fig. 4(c) is shown, how for an applied voltage of 30 V_{pp} , a strong displacement (28 nm) of the PMMA occurs just below the fluid channel in a pattern which creates an antisymmetric wave that leads to the formation of half standing wave inside the fluid channel with the pressure node

aligned vertically along the fluid center of magnitude 0.38 MPa. For application purposes, the more interesting quantity to study, is the acoustic radiation force acting on suspended microparticles in the fluid channel, as shown in Fig. 4(b) for $5\text{-}\mu\text{m}$ -diameter polystyrene particles as used in Ref. [20]. The maximum force obtained from the simulation is 3.9 pN in the bottom half of the microchannel, and it is seen how the horizontal component generally is larger than the vertical one. This is quantified by the figure of merit [21], defined as $R = \int_{V_{\text{fl}}} -\text{sign}(y)F_y^{\text{rad}} dV / \int_{V_{\text{fl}}} |F_z^{\text{rad}}| dV = 3.1$, a value comparable to the ones found in the ideal 2D cases studied in Ref. [21], and indicating a acoustophoretic ability of decent quality.

IX. SUMMARY AND CONCLUDING REMARKS

The core of the theory developed by Bach and Bruus [31] is the decomposition of the 1st- and 2nd-order acoustic fields into short-range boundary-layer fields, which vary on the length scale δ , and long-range bulk fields, which vary on the length scale of the inverse of wave number k_0^{-1} . This decomposition enables an analytical evaluation of the boundary layer field given the assumptions that the wall motion is small and the fluid-solid curvature is large. With these prerequisites, Bach and Bruus developed the BL18 model in terms of a slip-velocity boundary condition for the streaming velocity field valid to lowest order in the small parameter $k_0\delta \approx 0.003$. Since the BL18 model avoids to resolve the thin boundary layer numerically, it enables simulation of actual acoustofluidic devices in 3D. So far, the BL18 model has only been tested for (hard) glass and glass-Si devices [31, 35], but remarkably, we have demonstrated in this work, that for soft polymer-based devices, the higher order $k_0\delta$ terms, hitherto neglected in the BL18 model, must be included to obtain a quantitative correct description of (soft) polymer acoustofluidic devices, even in cases where the BL18 model fails to predict qualitative correct responses. We call this improved model the BL25 model.

In Sec. III B, the boundary condition derived for the 1st-order pressure p_1 in the BL25-model is identical to that of the BL18 model. However, in Sec. III C one extra term is added to the 1st-order stress-boundary condition in the BL25 model compared to the BL18, the first difference between the two models.

Going to the 2nd-order streaming field \mathbf{v}_2 , the two models differ more substantially. We found that for acoustically soft materials like polymers, it is important to include terms of one higher order in $k\delta$ than was done in the BL18 model, as the polymer wall velocity can be more than one order of magnitude larger than that of a hard glass or glass-Si device. In particular, the larger wall velocity facilitates a larger short-ranged perpendicular boundary-layer velocity component v_{2c}^{00} , resulting in the non-negligible influence of the higher-order terms in the short-range boundary-layer velocity $\mathbf{v}_2^{\delta 0}$ Eq. (35).

The main theoretical result of this work is the final form of the slip boundary condition Eq. (39) of the BL25 model, comprising a total of 25 terms for the long-range streaming field for $\mathbf{v}_2^{\delta 0}$, obtained by combining short-range velocity $\mathbf{v}_2^{\delta 0}$ and the Stokes drift velocity \mathbf{v}_2^{sd} , Eqs. (35) and (38).

The main modeling result is the implementation of the BL25 model in the finite-element method using the “**Weak Form PDE Interface**” of the software COMSOL Multiphysics, described in Sec. VI. Here, the detailed implementation of the tangential and perpendicular derivatives on the weakly-curved fluid-solid interface, which appears in the above mentioned boundary conditions, is essential.

Finally, the main simulation results are the numerical

and experimental validation of the BL25 model presented in Secs. VII and VIII based on the 3D and 2D models introduced in Sec. V and the experimental device described in Sec. VIII, all shown in Figs. 1 and 4, respectively. The first step in the numerical validation was the mesh convergence study presented in Sec. VII A, which revealed satisfactory convergence of the 1st- and 2nd-order fields in the BL25 model. In all cases, an asymptotic behavior approached exponentially was obtained for all fields as a function of refining the mesh.

The second numerical validation step was the comparison in 3D between the BL25 model and the Full model presented in Sec. VII B. This validation is not trivial as the main point in developing the BL25 model is to be able to perform 3D device simulation. However, by introducing a tiny sub-mm model device, still containing all the essential components of an acoustofluidic device, we were able to simulate the acoustofluidic response in both models by stretching our available computer resources to the limit. To our knowledge, this may be the first example of a Full-model simulation of an acoustofluidic device. This validation was successful, as we found the relative deviation between the models to be $\epsilon_2^{\text{1st}} \lesssim 0.5\%$ and $\epsilon_2^{\text{2nd}} \lesssim 2\%$ for the 1st- and 2nd-order fields, respectively.

The third numerical validation step, presented in Sec. VII C, was to compare simulation results in 2D of both the BL25 model and the BL18 model to the Full model. The results are summarized in Fig. 3 and Table III. The BL25 model predicts the results of the Full model with both qualitative and quantitative accuracy, with relative deviations from the Full model being at most 4 % in all shown cases, including both hard glass and soft PMMA devices being driven both on and off resonance. In contrast, the BL18 model only obtains the same good level of quantitative agreement with the Full model in the cases previously tested, hard devices run at resonance [31, 35], whereas large quantitative deviations are seen for soft polymer devices both on and off resonance, and somewhat surprising, also for hard glass devices run off resonance. Importantly, we even found cases where the predictions of the BL25 model matched the Full model, whereas the BL18 model predicted qualitative wrong responses, such as the example shown in Fig. 3(c2). In a final 2D numerical validation, we found that even in the case of devices with rectangular channel cross sections, where the four corners with their zero radius of curvature clearly violate the basic assumption of the BL25 and BL18 models that the curvature must be sufficiently large compared to the boundary-layer thickness δ , the BL25 model deviated very little from the Full model, whereas the BL18 model failed. Specifically, we found the relative deviations $\epsilon_2(v_2^{25}, v_2^{\text{F}}) = 4\%$ and $\epsilon_2(v_2^{18}, v_2^{\text{F}}) = 78\%$ in the (soft) PMMA device run at resonance. For a (hard) glass device at resonance, both models did better, with $\epsilon_2(v_2^{25}, v_2^{\text{F}}) = 0.4\%$ and $\epsilon_2(v_2^{18}, v_2^{\text{F}}) = 2\%$.

Finally, the experimental validation against published data in the literature by Lickert *et al.* [20] for a (soft)

PMMA device driven by a PZT Pz26 transducer presented in Sec. VIII, show that the BL25 model can predict the measured resonance frequency within 1 % and the measured electrical admittance of the loaded PZT Pz26 transducer as well as the acoustic energy density in the water-filled channel both qualitatively and quantitatively (within about 15 %). In this validation, the thickness of the glycerol 'glue' layer was the only fitting parameter. This is in contrast to the previous BL18 model results also published in Ref. [20], where the electrical admittance and the acoustic energy density deviated by nearly an order of magnitude from the experimental data. This experimental validation could be improved by knowing the specific clamping of the device in the sample holder and the actual thickness of the 'glue' layer.

Given the extensive validation simulations showing that the BL25 model is in good quantitative agreement (within 4 %) with the full model for both 1st- and 2nd-order fields and both on and off resonance, given the quantitative agreement (within 15 %) with experimental data, and given that the BL25 model in all cases performs better than the previous BL18 model, it appears to be justified to introduce the complex BL25 model comprising of the 25 terms in Eq. (39). It is worth mentioning that the computation time of the complex BL25 model is not significantly different from the more simple BL18 model. Based on the presented results, we believe that the BL25 model will be an important tool in future modeling of actual 3D acoustofluidic devices, both as a mean to unravel the intricate physical nature of such devices, and as part of design optimization for technological applications of such devices.

ACKNOWLEDGEMENTS

This work was supported by the *ACOUSOME* project funded by the European Innovation Council (EIC), *HORIZON EIC 2022 TRANSITION*, grant No. 101099787.

TABLE V. Parameters of the PZT transducer of type Pz26 [50] used in the numerical simulations of the experimental PMMA device [20] described in Sec. VIII.

Parameter	Symbol	Value	Unit
Mass density	ρ^{Pz}	7700	kg m ⁻³
Elastic modulus	C_{11}	168 - i3.36	GPa
Elastic modulus	C_{12}	110 - i2.20	GPa
Elastic modulus	C_{13}	99.9 - i2.00	GPa
Elastic modulus	C_{33}	123 - i2.46	GPa
Elastic modulus	C_{44}	30.1 - i0.60	GPa
Coupling constant	e_{15}	9.86 - i0.20	C m ⁻²
Coupling constant	e_{31}	-2.8 + i0.06	C m ⁻²
Coupling constant	e_{33}	14.7 - i0.29	C m ⁻²
Electric permittivity	ϵ_{11}	828(1 - i0.02)	ϵ_0 F m ⁻¹
Electric permittivity	ϵ_{33}	700(1 - i0.02)	ϵ_0 F m ⁻¹

Appendix A: The constitutive equations for the piezoelectric transducers

The constitutive equations for the three types of piezoelectric transducers used in this work all have the same form. In the Voigt notation, the six independent components σ_{1ik}^{Pz} of the symmetric stress tensor $\boldsymbol{\sigma}_1^{\text{Pz}}$ and $s_{1ik}^{\text{Pz}} = \frac{1}{2}(\partial_i u_{1k} + \partial_k u_{1i})$ of the symmetric strain tensor $\boldsymbol{s}_1^{\text{Pz}}$ are represented by the six-dimensional Voigt vectors $\boldsymbol{\sigma}_1^{\text{V}}$ and $\boldsymbol{s}_1^{\text{V}}$, whose transposed forms are

$$[\boldsymbol{\sigma}_1^{\text{V}}]^\top = \{\sigma_{1xx}^{\text{Pz}}, \sigma_{1yy}^{\text{Pz}}, \sigma_{1zz}^{\text{Pz}}, \sigma_{1yz}^{\text{Pz}}, \sigma_{1xz}^{\text{Pz}}, \sigma_{1xy}^{\text{Pz}}\}, \quad (\text{A1a})$$

$$[\boldsymbol{s}_1^{\text{V}}]^\top = \{s_{1xx}^{\text{Pz}}, s_{1yy}^{\text{Pz}}, s_{1zz}^{\text{Pz}}, 2s_{1yz}^{\text{Pz}}, 2s_{1xz}^{\text{Pz}}, 2s_{1xy}^{\text{Pz}}\}. \quad (\text{A1b})$$

These mechanical fields are supplemented by the electrical potential φ_1 and its gradient, the electric field $\boldsymbol{E}_1 = -\nabla\varphi_1$, as well as the electric displacement field \boldsymbol{D}_1 . The Voigt representation of the constitutive equations for the piezoelectric transducers in a 9×9 -matrix equation relating $\boldsymbol{\sigma}_1^{\text{V}}$ and \boldsymbol{D}_1 to $\boldsymbol{s}_1^{\text{V}}$ and $-\nabla\varphi_1$,

$$\begin{pmatrix} \boldsymbol{\sigma}_1^{\text{V}} \\ \boldsymbol{D}_1 \end{pmatrix} = \boldsymbol{M} \cdot \begin{pmatrix} \boldsymbol{s}_1^{\text{V}} \\ -\nabla\varphi_1 \end{pmatrix}, \quad (\text{A2})$$

$$\boldsymbol{M} = \begin{pmatrix} C_{11} & C_{12} & C_{13} & 0 & 0 & 0 & 0 & 0 & -e_{31} \\ C_{12} & C_{11} & C_{13} & 0 & 0 & 0 & 0 & 0 & -e_{31} \\ C_{13} & C_{13} & C_{33} & 0 & 0 & 0 & 0 & 0 & -e_{33} \\ 0 & 0 & 0 & C_{44} & 0 & 0 & 0 & -e_{15} & 0 \\ 0 & 0 & 0 & 0 & C_{44} & 0 & -e_{15} & 0 & 0 \\ 0 & 0 & 0 & 0 & 0 & C_{66} & 0 & 0 & 0 \\ 0 & 0 & 0 & 0 & e_{15} & 0 & \epsilon_{11} & 0 & 0 \\ 0 & 0 & 0 & e_{15} & 0 & 0 & 0 & \epsilon_{11} & 0 \\ e_{31} & e_{31} & e_{33} & 0 & 0 & 0 & 0 & 0 & \epsilon_{33} \end{pmatrix}.$$

The parameter values of the piezoelectric transducers used in this work are given in Table II for Al_{0.6}Sc_{0.4}N and PZT Pz27, and in Table V for PZT Pz26.

Appendix B: 2nd-order boundary-layer fields

In this Appendix, we compute the 2nd-order, time-averaged, boundary-layer fields pressure p_2^δ and velocity \boldsymbol{v}_2^δ in the fluid, based on the 1st- and 2nd-order expressions given in Secs. III and IV. Following Eq. (28a), the velocity field is split in two components, $\boldsymbol{v}_2^{\delta 0} = \boldsymbol{v}_2^{\delta p} + \boldsymbol{v}_2^{\delta v}$, that are treated independently.

1. Computation of p_2^δ

To obtain the coordinate-separated form of the source term ∇p_2^δ in Eq. (28), we first take the divergence of

Eq. (27), neglect the $\nabla \cdot \mathbf{v}_2^\delta$ -terms of order Γ , and finally use $\nabla^2 p_2^\delta \approx \partial_\zeta^2 p_2^\delta$, to arrive at

$$\partial_\zeta^2 p_2^\delta = -\rho_0 \nabla \cdot [\nabla \cdot \langle \mathbf{v}_1^\delta \mathbf{v}_1^\delta + \mathbf{v}_1^d \mathbf{v}_1^\delta + \mathbf{v}_1^\delta \mathbf{v}_1^d \rangle]. \quad (\text{B1})$$

Then the coordinate-separated form of this expression is obtained by using Eqs. (31d) and (32), and we arrive at the following 20-term expression for $\partial_\zeta^2 p_2^\delta$,

$$\begin{aligned} \partial_\zeta^2 p_2^\delta = & -\rho_0 \left\{ \right. & (\text{B2}) \\ & + \nabla_{\parallel} \cdot [\nabla_{\parallel} \cdot \langle I_{qq}^{(0)} \mathbf{v}_{1\parallel}^{\delta 0}, \mathbf{v}_{1\parallel}^{\delta 0} \rangle] + \langle I_{qq}^{(-2)} v_{1\zeta}^{\delta 0}, v_{1\zeta}^{\delta 0*} \rangle \\ & + \nabla_{\parallel} \cdot [\langle I_{qq}^{(-1)} \mathbf{v}_{1\parallel}^{\delta 0}, v_{1\zeta}^{\delta 0} \rangle + \langle I_{qq}^{(-1)} v_{1\zeta}^{\delta 0}, \mathbf{v}_{1\parallel}^{\delta 0} \rangle] \\ & + \nabla_{\parallel} \cdot [\nabla_{\parallel} \cdot \langle I_{1q}^{(0)} \mathbf{v}_{1\parallel}^{d0}, \mathbf{v}_{1\parallel}^{\delta 0} \rangle] + I_{1q}^{(-2)} (v_{1\zeta}^{d0} v_{1\zeta}^{\delta 0}) \\ & + \nabla_{\parallel} \cdot [\langle I_{1q}^{(-1)} \mathbf{v}_{1\parallel}^{d0}, v_{1\zeta}^{\delta 0} \rangle + \langle I_{1q}^{(-1)} v_{1\zeta}^{d0}, \mathbf{v}_{1\parallel}^{\delta 0} \rangle] \\ & + \nabla_{\parallel} \cdot [\nabla_{\parallel} \cdot \langle I_{\zeta q}^{(0)} \partial_\zeta \mathbf{v}_{1\parallel}^{d0}, \mathbf{v}_{1\parallel}^{\delta 0} \rangle] + \langle I_{\zeta q}^{(-2)} \partial_\zeta v_{1\zeta}^{d0}, v_{1\zeta}^{\delta 0} \rangle \\ & + \nabla_{\parallel} \cdot [\langle I_{\zeta q}^{(-1)} \partial_\zeta \mathbf{v}_{1\parallel}^{d0}, v_{1\zeta}^{\delta 0} \rangle + \langle I_{\zeta q}^{(-1)} \partial_\zeta v_{1\zeta}^{d0}, \mathbf{v}_{1\parallel}^{\delta 0} \rangle] \\ & + \nabla_{\parallel} \cdot [\nabla_{\parallel} \cdot \langle I_{q1}^{(0)} \mathbf{v}_{1\parallel}^{\delta 0}, \mathbf{v}_{1\parallel}^{d0} \rangle] + \langle I_{q1}^{(-2)} v_{1\zeta}^{\delta 0}, v_{1\zeta}^{d0} \rangle \\ & + \nabla_{\parallel} \cdot [\langle I_{q1}^{(-1)} \mathbf{v}_{1\parallel}^{\delta 0}, v_{1\zeta}^{d0} \rangle + \langle I_{q1}^{(-1)} v_{1\zeta}^{\delta 0}, \mathbf{v}_{1\parallel}^{d0} \rangle] \\ & + \nabla_{\parallel} \cdot [\nabla_{\parallel} \cdot \langle I_{q\zeta}^{(0)} \mathbf{v}_{1\parallel}^{\delta 0}, \partial_\zeta \mathbf{v}_{1\parallel}^{d0} \rangle] + \langle I_{q\zeta}^{(-2)} v_{1\zeta}^{\delta 0}, \partial_\zeta v_{1\zeta}^{d0} \rangle \\ & \left. + \nabla_{\parallel} \cdot [\langle I_{q\zeta}^{(-1)} \mathbf{v}_{1\parallel}^{\delta 0}, \partial_\zeta v_{1\zeta}^{d0} \rangle + \langle I_{q\zeta}^{(-1)} v_{1\zeta}^{\delta 0}, \partial_\zeta \mathbf{v}_{1\parallel}^{d0} \rangle] \right\}. \end{aligned}$$

The short-range pressure p_2^δ is obtained from $\partial_\zeta^2 p_2^\delta$ by integrating twice with respect to ζ . This amounts to the trivial substitution of $I_{ab}^{(n)}$ in Eq. (B2) by $I_{ab}^{(n+2)}$,

$$\begin{aligned} p_2^\delta = & -\rho_0 \left\{ \right. & (\text{B3}) \\ & + \nabla_{\parallel} \cdot [\nabla_{\parallel} \cdot \langle I_{qq}^{(2)} \mathbf{v}_{1\parallel}^{\delta 0}, \mathbf{v}_{1\parallel}^{\delta 0} \rangle] + \langle I_{qq}^{(0)} v_{1\zeta}^{\delta 0}, v_{1\zeta}^{\delta 0} \rangle \\ & + \nabla_{\parallel} \cdot [\langle I_{qq}^{(1)} \mathbf{v}_{1\parallel}^{\delta 0}, v_{1\zeta}^{\delta 0} \rangle + \langle I_{qq}^{(1)} v_{1\zeta}^{\delta 0}, \mathbf{v}_{1\parallel}^{\delta 0} \rangle] \\ & + \nabla_{\parallel} \cdot [\nabla_{\parallel} \cdot \langle I_{1q}^{(2)} \mathbf{v}_{1\parallel}^{d0}, \mathbf{v}_{1\parallel}^{\delta 0} \rangle] + I_{1q}^{(0)} (v_{1\zeta}^{d0} v_{1\zeta}^{\delta 0}) \\ & + \nabla_{\parallel} \cdot [\langle I_{1q}^{(1)} \mathbf{v}_{1\parallel}^{d0}, v_{1\zeta}^{\delta 0} \rangle + \langle I_{1q}^{(1)} v_{1\zeta}^{d0}, \mathbf{v}_{1\parallel}^{\delta 0} \rangle] \\ & + \nabla_{\parallel} \cdot [\nabla_{\parallel} \cdot \langle I_{\zeta q}^{(2)} \partial_\zeta \mathbf{v}_{1\parallel}^{d0}, \mathbf{v}_{1\parallel}^{\delta 0} \rangle] + \langle I_{\zeta q}^{(0)} \partial_\zeta v_{1\zeta}^{d0}, v_{1\zeta}^{\delta 0} \rangle \\ & + \nabla_{\parallel} \cdot [\langle I_{\zeta q}^{(1)} \partial_\zeta \mathbf{v}_{1\parallel}^{d0}, v_{1\zeta}^{\delta 0} \rangle + \langle I_{\zeta q}^{(1)} \partial_\zeta v_{1\zeta}^{d0}, \mathbf{v}_{1\parallel}^{\delta 0} \rangle] \\ & + \nabla_{\parallel} \cdot [\nabla_{\parallel} \cdot \langle I_{q1}^{(2)} \mathbf{v}_{1\parallel}^{\delta 0}, \mathbf{v}_{1\parallel}^{d0} \rangle] + \langle I_{q1}^{(0)} v_{1\zeta}^{\delta 0}, v_{1\zeta}^{d0} \rangle \\ & + \nabla_{\parallel} \cdot [\langle I_{q1}^{(1)} \mathbf{v}_{1\parallel}^{\delta 0}, v_{1\zeta}^{d0} \rangle + \langle I_{q1}^{(1)} v_{1\zeta}^{\delta 0}, \mathbf{v}_{1\parallel}^{d0} \rangle] \\ & + \nabla_{\parallel} \cdot [\nabla_{\parallel} \cdot \langle I_{q\zeta}^{(2)} \mathbf{v}_{1\parallel}^{\delta 0}, \partial_\zeta \mathbf{v}_{1\parallel}^{d0} \rangle] + \langle I_{q\zeta}^{(0)} v_{1\zeta}^{\delta 0}, \partial_\zeta v_{1\zeta}^{d0} \rangle \\ & \left. + \nabla_{\parallel} \cdot [\langle I_{q\zeta}^{(1)} \mathbf{v}_{1\parallel}^{\delta 0}, \partial_\zeta v_{1\zeta}^{d0} \rangle + \langle I_{q\zeta}^{(1)} v_{1\zeta}^{\delta 0}, \partial_\zeta \mathbf{v}_{1\parallel}^{d0} \rangle] \right\}. \end{aligned}$$

2. Computation of $\mathbf{v}_2^{\delta p}$

The parallel component $\mathbf{v}_{2\parallel}^{\delta p}$ and perpendicular component $v_{2\zeta}^{\delta p}$ of the boundary-layer velocity $\mathbf{v}_2^{\delta p}$ are obtained by integration of Eq. (28b),

$$\partial_\zeta^2 \mathbf{v}_{2\parallel}^{\delta p} = \nabla_{\parallel} \frac{p_2^\delta}{\eta_0} \Rightarrow \mathbf{v}_{2\parallel}^{\delta p}(\zeta) = \nabla_{\parallel} \int^\zeta \int^{\zeta'} \frac{p_2^\delta(\zeta'')}{\eta_0} d\zeta'' d\zeta', \quad (\text{B4a})$$

$$\partial_\zeta^2 v_{2\zeta}^{\delta p} = \partial_\zeta \frac{p_2^\delta}{\eta_0} \Rightarrow v_{2\zeta}^{\delta p}(\zeta) = \int^\zeta \frac{p_2^\delta(\zeta')}{\eta_0} d\zeta'. \quad (\text{B4b})$$

The computation of $\mathbf{v}_{2\parallel}^{\delta p}$ ($v_{2\zeta}^{\delta p}$) involves integration of p_2^δ twice (once) with respect of ζ , which according to Eq. (30b) amounts to increasing the superscript in all factors $I_{ab}^{(n)}$ by 2 (by 1). Inserting p_2^δ from Eq. (B3) into Eqs. (B4a) and (B4b) leads to

$$\begin{aligned} \mathbf{v}_{2\parallel}^{\delta p} = & -\frac{1}{\nu_0} \nabla_{\parallel} \left\{ \right. & (\text{B5}) \\ & + \nabla_{\parallel} \cdot [\nabla_{\parallel} \cdot \langle I_{qq}^{(4)} \mathbf{v}_{1\parallel}^{\delta 0}, \mathbf{v}_{1\parallel}^{\delta 0} \rangle] + \langle I_{qq}^{(2)} v_{1\zeta}^{\delta 0}, v_{1\zeta}^{\delta 0} \rangle \\ & + \nabla_{\parallel} \cdot [\langle I_{qq}^{(3)} \mathbf{v}_{1\parallel}^{\delta 0}, v_{1\zeta}^{\delta 0} \rangle + \langle I_{qq}^{(3)} v_{1\zeta}^{\delta 0}, \mathbf{v}_{1\parallel}^{\delta 0} \rangle] \\ & + \nabla_{\parallel} \cdot [\nabla_{\parallel} \cdot \langle I_{1q}^{(4)} \mathbf{v}_{1\parallel}^{d0}, \mathbf{v}_{1\parallel}^{\delta 0} \rangle] + I_{1q}^{(2)} (v_{1\zeta}^{d0} v_{1\zeta}^{\delta 0}) \\ & + \nabla_{\parallel} \cdot [\langle I_{1q}^{(3)} \mathbf{v}_{1\parallel}^{d0}, v_{1\zeta}^{\delta 0} \rangle + \langle I_{1q}^{(3)} v_{1\zeta}^{d0}, \mathbf{v}_{1\parallel}^{\delta 0} \rangle] \\ & + \nabla_{\parallel} \cdot [\nabla_{\parallel} \cdot \langle I_{\zeta q}^{(4)} \partial_\zeta \mathbf{v}_{1\parallel}^{d0}, \mathbf{v}_{1\parallel}^{\delta 0} \rangle] + \langle I_{\zeta q}^{(2)} \partial_\zeta v_{1\zeta}^{d0}, v_{1\zeta}^{\delta 0} \rangle \\ & + \nabla_{\parallel} \cdot [\langle I_{\zeta q}^{(3)} \partial_\zeta \mathbf{v}_{1\parallel}^{d0}, v_{1\zeta}^{\delta 0} \rangle + \langle I_{\zeta q}^{(3)} \partial_\zeta v_{1\zeta}^{d0}, \mathbf{v}_{1\parallel}^{\delta 0} \rangle] \\ & + \nabla_{\parallel} \cdot [\nabla_{\parallel} \cdot \langle I_{q1}^{(4)} \mathbf{v}_{1\parallel}^{\delta 0}, \mathbf{v}_{1\parallel}^{d0} \rangle] + \langle I_{q1}^{(2)} v_{1\zeta}^{\delta 0}, v_{1\zeta}^{d0} \rangle \\ & + \nabla_{\parallel} \cdot [\langle I_{q1}^{(3)} \mathbf{v}_{1\parallel}^{\delta 0}, v_{1\zeta}^{d0} \rangle + \langle I_{q1}^{(3)} v_{1\zeta}^{\delta 0}, \mathbf{v}_{1\parallel}^{d0} \rangle] \\ & + \nabla_{\parallel} \cdot [\nabla_{\parallel} \cdot \langle I_{q\zeta}^{(4)} \mathbf{v}_{1\parallel}^{\delta 0}, \partial_\zeta \mathbf{v}_{1\parallel}^{d0} \rangle] + \langle I_{q\zeta}^{(2)} v_{1\zeta}^{\delta 0}, \partial_\zeta v_{1\zeta}^{d0} \rangle \\ & \left. + \nabla_{\parallel} \cdot [\langle I_{q\zeta}^{(3)} \mathbf{v}_{1\parallel}^{\delta 0}, \partial_\zeta v_{1\zeta}^{d0} \rangle + \langle I_{q\zeta}^{(3)} v_{1\zeta}^{\delta 0}, \partial_\zeta \mathbf{v}_{1\parallel}^{d0} \rangle] \right\}. \end{aligned}$$

and

$$\begin{aligned} v_{2\zeta}^{\delta p} = & -\frac{1}{\nu_0} \left\{ \right. & (\text{B6}) \\ & + \nabla_{\parallel} \cdot [\nabla_{\parallel} \cdot \langle I_{qq}^{(3)} \mathbf{v}_{1\parallel}^{\delta 0}, \mathbf{v}_{1\parallel}^{\delta 0} \rangle] + \langle I_{qq}^{(1)} v_{1\zeta}^{\delta 0}, v_{1\zeta}^{\delta 0} \rangle \\ & + \nabla_{\parallel} \cdot [\langle I_{qq}^{(2)} \mathbf{v}_{1\parallel}^{\delta 0}, v_{1\zeta}^{\delta 0} \rangle + \langle I_{qq}^{(2)} v_{1\zeta}^{\delta 0}, \mathbf{v}_{1\parallel}^{\delta 0} \rangle] \\ & + \nabla_{\parallel} \cdot [\nabla_{\parallel} \cdot \langle I_{1q}^{(3)} \mathbf{v}_{1\parallel}^{d0}, \mathbf{v}_{1\parallel}^{\delta 0} \rangle] + \langle I_{1q}^{(1)} v_{1\zeta}^{d0}, v_{1\zeta}^{\delta 0} \rangle \\ & + \nabla_{\parallel} \cdot [\langle I_{1q}^{(2)} \mathbf{v}_{1\parallel}^{d0}, v_{1\zeta}^{\delta 0} \rangle + \langle I_{1q}^{(2)} v_{1\zeta}^{d0}, \mathbf{v}_{1\parallel}^{\delta 0} \rangle] \\ & + \nabla_{\parallel} \cdot [\nabla_{\parallel} \cdot \langle I_{\zeta q}^{(3)} \partial_\zeta \mathbf{v}_{1\parallel}^{d0}, \mathbf{v}_{1\parallel}^{\delta 0} \rangle] + \langle I_{\zeta q}^{(1)} \partial_\zeta v_{1\zeta}^{d0}, v_{1\zeta}^{\delta 0} \rangle \\ & + \nabla_{\parallel} \cdot [\langle I_{\zeta q}^{(2)} \partial_\zeta \mathbf{v}_{1\parallel}^{d0}, v_{1\zeta}^{\delta 0} \rangle + \langle I_{\zeta q}^{(2)} \partial_\zeta v_{1\zeta}^{d0}, \mathbf{v}_{1\parallel}^{\delta 0} \rangle] \\ & + \nabla_{\parallel} \cdot [\nabla_{\parallel} \cdot \langle I_{q1}^{(3)} \mathbf{v}_{1\parallel}^{\delta 0}, \mathbf{v}_{1\parallel}^{d0} \rangle] + \langle I_{q1}^{(1)} v_{1\zeta}^{\delta 0}, v_{1\zeta}^{d0} \rangle \\ & + \nabla_{\parallel} \cdot [\langle I_{q1}^{(2)} \mathbf{v}_{1\parallel}^{\delta 0}, v_{1\zeta}^{d0} \rangle + \langle I_{q1}^{(2)} v_{1\zeta}^{\delta 0}, \mathbf{v}_{1\parallel}^{d0} \rangle] \\ & + \nabla_{\parallel} \cdot [\nabla_{\parallel} \cdot \langle I_{q\zeta}^{(3)} \mathbf{v}_{1\parallel}^{\delta 0}, \partial_\zeta \mathbf{v}_{1\parallel}^{d0} \rangle] + \langle I_{q\zeta}^{(1)} v_{1\zeta}^{\delta 0}, \partial_\zeta v_{1\zeta}^{d0} \rangle \\ & \left. + \nabla_{\parallel} \cdot [\langle I_{q\zeta}^{(2)} \mathbf{v}_{1\parallel}^{\delta 0}, \partial_\zeta v_{1\zeta}^{d0} \rangle + \langle I_{q\zeta}^{(2)} v_{1\zeta}^{\delta 0}, \partial_\zeta \mathbf{v}_{1\parallel}^{d0} \rangle] \right\}. \end{aligned}$$

3. Computation of $v_2^{\delta v}$

To determine $v_2^{\delta v}$, we compute the coordinate-separated form of the source term in Eq. (28) by using Eqs. (31a) and (32),

$$\begin{aligned} \partial_\zeta^2 v_2^{\delta v} &= \frac{1}{\nu_0} \nabla \cdot \langle \mathbf{v}_1^\delta \mathbf{v}_1^\delta + \mathbf{v}_1^d \mathbf{v}_1^d + \mathbf{v}_1^\delta \mathbf{v}_1^d \rangle \quad (\text{B7}) \\ &= \frac{1}{\nu_0} \left\{ \nabla_{\parallel} \cdot \langle I_{qq}^{(0)} \mathbf{v}_1^{\delta 0}, \mathbf{v}_1^{\delta 0} \rangle + \langle I_{qq}^{(-1)} \mathbf{v}_1^{\delta 0}, v_{1\zeta}^{\delta 0} \rangle \right. \\ &\quad + \nabla_{\parallel} \cdot \langle I_{1q}^{(0)} \mathbf{v}_1^{d0}, \mathbf{v}_1^{\delta 0} \rangle + \langle I_{1q}^{(-1)} \mathbf{v}_1^{d0}, v_{1\zeta}^{\delta 0} \rangle \\ &\quad + \nabla_{\parallel} \cdot \langle I_{\zeta q}^{(0)} \partial_\zeta \mathbf{v}_1^{d0}, \mathbf{v}_1^{\delta 0} \rangle + \langle I_{\zeta q}^{(-1)} \partial_\zeta \mathbf{v}_1^{d0}, v_{1\zeta}^{\delta 0} \rangle \\ &\quad + \nabla_{\parallel} \cdot \langle I_{q1}^{(0)} \mathbf{v}_1^{\delta 0}, \mathbf{v}_1^{d0} \rangle + \langle I_{q1}^{(-1)} \mathbf{v}_1^{\delta 0}, v_{1\zeta}^{d0} \rangle \\ &\quad \left. + \nabla_{\parallel} \cdot \langle I_{q\zeta}^{(0)} \mathbf{v}_1^{\delta 0}, \partial_\zeta \mathbf{v}_1^{d0} \rangle + \langle I_{q\zeta}^{(-1)} \mathbf{v}_1^{\delta 0}, \partial_\zeta v_{1\zeta}^{d0} \rangle \right\}. \end{aligned}$$

From this, $v_2^{\delta v}$ is found by integrating twice after ζ , which according to Eq. (30b) amounts to increase the superscript in all factors $I_{ab}^{(n)}$ by 2, which results in

$$\begin{aligned} v_2^{\delta v} &= \frac{1}{\nu_0} \left\{ \nabla_{\parallel} \cdot \langle I_{qq}^{(2)} \mathbf{v}_1^{\delta 0}, \mathbf{v}_1^{\delta 0} \rangle + \langle I_{qq}^{(1)} \mathbf{v}_1^{\delta 0}, v_{1\zeta}^{\delta 0} \rangle \quad (\text{B8}) \right. \\ &\quad + \nabla_{\parallel} \cdot \langle I_{1q}^{(2)} \mathbf{v}_1^{d0}, \mathbf{v}_1^{\delta 0} \rangle + \langle I_{1q}^{(1)} \mathbf{v}_1^{d0}, v_{1\zeta}^{\delta 0} \rangle \\ &\quad + \nabla_{\parallel} \cdot \langle I_{\zeta q}^{(2)} \partial_\zeta \mathbf{v}_1^{d0}, \mathbf{v}_1^{\delta 0} \rangle + \langle I_{\zeta q}^{(1)} \partial_\zeta \mathbf{v}_1^{d0}, v_{1\zeta}^{\delta 0} \rangle \\ &\quad + \nabla_{\parallel} \cdot \langle I_{q1}^{(2)} \mathbf{v}_1^{\delta 0}, \mathbf{v}_1^{d0} \rangle + \langle I_{q1}^{(1)} \mathbf{v}_1^{\delta 0}, v_{1\zeta}^{d0} \rangle \\ &\quad \left. + \nabla_{\parallel} \cdot \langle I_{q\zeta}^{(2)} \mathbf{v}_1^{\delta 0}, \partial_\zeta \mathbf{v}_1^{d0} \rangle + \langle I_{q\zeta}^{(1)} \mathbf{v}_1^{\delta 0}, \partial_\zeta v_{1\zeta}^{d0} \rangle \right\}. \end{aligned}$$

Splitting this into the parallel and perpendicular components $v_{2\parallel}^{\delta v}$ and $v_{2\zeta}^{\delta v}$, respectively, yields,

$$\begin{aligned} v_{2\parallel}^{\delta v} &= \frac{1}{\nu_0} \left\{ \nabla_{\parallel} \cdot \langle I_{qq}^{(2)} \mathbf{v}_{1\parallel}^{\delta 0}, \mathbf{v}_{1\parallel}^{\delta 0} \rangle + \langle I_{qq}^{(1)} \mathbf{v}_{1\parallel}^{\delta 0}, v_{1\zeta}^{\delta 0} \rangle \quad (\text{B9}) \right. \\ &\quad + \nabla_{\parallel} \cdot \langle I_{1q}^{(2)} \mathbf{v}_{1\parallel}^{d0}, \mathbf{v}_{1\parallel}^{\delta 0} \rangle + \langle I_{1q}^{(1)} \mathbf{v}_{1\parallel}^{d0}, v_{1\zeta}^{\delta 0} \rangle \\ &\quad + \nabla_{\parallel} \cdot \langle I_{\zeta q}^{(2)} \partial_\zeta \mathbf{v}_{1\parallel}^{d0}, \mathbf{v}_{1\parallel}^{\delta 0} \rangle + \langle I_{\zeta q}^{(1)} \partial_\zeta \mathbf{v}_{1\parallel}^{d0}, v_{1\zeta}^{\delta 0} \rangle \\ &\quad + \nabla_{\parallel} \cdot \langle I_{q1}^{(2)} \mathbf{v}_{1\parallel}^{\delta 0}, \mathbf{v}_{1\parallel}^{d0} \rangle + \langle I_{q1}^{(1)} \mathbf{v}_{1\parallel}^{\delta 0}, v_{1\zeta}^{d0} \rangle \\ &\quad \left. + \nabla_{\parallel} \cdot \langle I_{q\zeta}^{(2)} \mathbf{v}_{1\parallel}^{\delta 0}, \partial_\zeta \mathbf{v}_{1\parallel}^{d0} \rangle + \langle I_{q\zeta}^{(1)} \mathbf{v}_{1\parallel}^{\delta 0}, \partial_\zeta v_{1\zeta}^{d0} \rangle \right\}, \end{aligned}$$

$$\begin{aligned} v_{2\zeta}^{\delta v} &= \frac{1}{\nu_0} \left\{ \nabla_{\parallel} \cdot \langle I_{qq}^{(2)} v_{1\zeta}^{\delta 0}, \mathbf{v}_{1\parallel}^{\delta 0} \rangle + \langle I_{qq}^{(1)} v_{1\zeta}^{\delta 0}, v_{1\zeta}^{\delta 0} \rangle \quad (\text{B10}) \right. \\ &\quad + \nabla_{\parallel} \cdot \langle I_{1q}^{(2)} v_{1\zeta}^{d0}, \mathbf{v}_{1\parallel}^{\delta 0} \rangle + \langle I_{1q}^{(1)} v_{1\zeta}^{d0}, v_{1\zeta}^{\delta 0} \rangle \\ &\quad + \nabla_{\parallel} \cdot \langle I_{\zeta q}^{(2)} \partial_\zeta v_{1\zeta}^{d0}, \mathbf{v}_{1\parallel}^{\delta 0} \rangle + \langle I_{\zeta q}^{(1)} \partial_\zeta v_{1\zeta}^{d0}, v_{1\zeta}^{\delta 0} \rangle \\ &\quad + \nabla_{\parallel} \cdot \langle I_{q1}^{(2)} v_{1\zeta}^{\delta 0}, \mathbf{v}_{1\parallel}^{d0} \rangle + \langle I_{q1}^{(1)} v_{1\zeta}^{\delta 0}, v_{1\zeta}^{d0} \rangle \\ &\quad \left. + \nabla_{\parallel} \cdot \langle I_{q\zeta}^{(2)} v_{1\zeta}^{\delta 0}, \partial_\zeta \mathbf{v}_{1\parallel}^{d0} \rangle + \langle I_{q\zeta}^{(1)} v_{1\zeta}^{\delta 0}, \partial_\zeta v_{1\zeta}^{d0} \rangle \right\}. \end{aligned}$$

Adding Eqs. (B6) and (B10), gives the full $v_{2\zeta}^{\delta v}$,

$$\begin{aligned} v_{2\zeta}^{\delta v} &= v_{2\zeta}^{\delta p} + v_{2\zeta}^{\delta v} = -\frac{1}{\nu_0} \left\{ \quad (\text{B11}) \right. \\ &\quad + \nabla_{\parallel} \cdot [\nabla_{\parallel} \cdot \langle I_{qq}^{(3)} \mathbf{v}_{1\parallel}^{\delta 0}, \mathbf{v}_{1\parallel}^{\delta 0} \rangle] + \nabla_{\parallel} \cdot \langle I_{qq}^{(2)} \mathbf{v}_{1\parallel}^{\delta 0}, v_{1\zeta}^{\delta 0} \rangle \\ &\quad + \nabla_{\parallel} \cdot [\nabla_{\parallel} \cdot \langle I_{1q}^{(3)} \mathbf{v}_{1\parallel}^{d0}, \mathbf{v}_{1\parallel}^{\delta 0} \rangle] + \nabla_{\parallel} \cdot \langle I_{1q}^{(2)} \mathbf{v}_{1\parallel}^{d0}, v_{1\zeta}^{\delta 0} \rangle \\ &\quad + \nabla_{\parallel} \cdot [\nabla_{\parallel} \cdot \langle I_{\zeta q}^{(3)} \partial_\zeta \mathbf{v}_{1\parallel}^{d0}, \mathbf{v}_{1\parallel}^{\delta 0} \rangle] + \nabla_{\parallel} \cdot \langle I_{\zeta q}^{(2)} \partial_\zeta \mathbf{v}_{1\parallel}^{d0}, v_{1\zeta}^{\delta 0} \rangle \\ &\quad + \nabla_{\parallel} \cdot [\nabla_{\parallel} \cdot \langle I_{q1}^{(3)} \mathbf{v}_{1\parallel}^{\delta 0}, \mathbf{v}_{1\parallel}^{d0} \rangle] + \nabla_{\parallel} \cdot \langle I_{q1}^{(2)} \mathbf{v}_{1\parallel}^{\delta 0}, v_{1\zeta}^{d0} \rangle \\ &\quad \left. + \nabla_{\parallel} \cdot [\nabla_{\parallel} \cdot \langle I_{q\zeta}^{(3)} \mathbf{v}_{1\parallel}^{\delta 0}, \partial_\zeta \mathbf{v}_{1\parallel}^{d0} \rangle] + \nabla_{\parallel} \cdot \langle I_{q\zeta}^{(2)} \mathbf{v}_{1\parallel}^{\delta 0}, \partial_\zeta v_{1\zeta}^{d0} \rangle \right\}. \end{aligned}$$

4. The final expression for $v_2^{\delta 0}$

Using the scalings $\frac{2}{\omega \delta^2} \hat{I}_{qq}^{(n)}, \frac{2}{\omega \delta^2} \hat{I}_{1q}^{(n)} \propto \delta^{n-2}$ and $\frac{2}{\omega \delta^2} \hat{I}_{\zeta q}^{(n)} \propto \delta^{n-1}$ obtained from Eq. (33), we neglect the terms of higher order in δ and obtain,

$$\mathbf{v}_2^{\delta 0} = \mathbf{v}_{2\parallel}^{\delta 0} + v_{2\zeta}^{\delta 0} \mathbf{e}_\zeta = \mathbf{v}_{2\parallel}^{\delta p0} + \mathbf{v}_{2\parallel}^{\delta v0} + v_{2\zeta}^{\delta 0} \mathbf{e}_\zeta, \quad (\text{B12a})$$

$$\mathbf{v}_{2\parallel}^{\delta p0} = -\frac{2}{\omega \delta^2} \nabla_{\parallel} \left\{ \quad (\text{B12b}) \right.$$

$$\begin{aligned} &\quad + \nabla_{\parallel} \cdot [\nabla_{\parallel} \cdot \langle \hat{I}_{qq}^{(4)} \mathbf{v}_{1\parallel}^{\delta 0}, \mathbf{v}_{1\parallel}^{\delta 0} \rangle] + \langle \hat{I}_{qq}^{(2)} v_{1\zeta}^{\delta 0}, v_{1\zeta}^{\delta 0} \rangle \\ &\quad + \nabla_{\parallel} \cdot [\langle \hat{I}_{qq}^{(3)} \mathbf{v}_{1\parallel}^{\delta 0}, v_{1\zeta}^{\delta 0} \rangle + \langle \hat{I}_{qq}^{(3)} v_{1\zeta}^{\delta 0}, \mathbf{v}_{1\parallel}^{\delta 0} \rangle] \\ &\quad + \nabla_{\parallel} \cdot [\nabla_{\parallel} \cdot \langle \hat{I}_{1q}^{(4)} \mathbf{v}_{1\parallel}^{d0}, \mathbf{v}_{1\parallel}^{\delta 0} \rangle] + \langle \hat{I}_{1q}^{(2)} v_{1\zeta}^{d0}, v_{1\zeta}^{\delta 0} \rangle \\ &\quad + \nabla_{\parallel} \cdot [\langle \hat{I}_{1q}^{(3)} \mathbf{v}_{1\parallel}^{d0}, v_{1\zeta}^{\delta 0} \rangle + \langle \hat{I}_{1q}^{(3)} v_{1\zeta}^{d0}, \mathbf{v}_{1\parallel}^{\delta 0} \rangle] \\ &\quad + \nabla_{\parallel} \cdot [\nabla_{\parallel} \cdot \langle \hat{I}_{\zeta q}^{(4)} \partial_\zeta \mathbf{v}_{1\parallel}^{d0}, \mathbf{v}_{1\parallel}^{\delta 0} \rangle] + \langle \hat{I}_{\zeta q}^{(2)} \partial_\zeta v_{1\zeta}^{d0}, v_{1\zeta}^{\delta 0} \rangle \\ &\quad + \nabla_{\parallel} \cdot [\langle \hat{I}_{\zeta q}^{(3)} \partial_\zeta \mathbf{v}_{1\parallel}^{d0}, v_{1\zeta}^{\delta 0} \rangle + \langle \hat{I}_{\zeta q}^{(3)} \partial_\zeta v_{1\zeta}^{d0}, \mathbf{v}_{1\parallel}^{\delta 0} \rangle] \\ &\quad + \nabla_{\parallel} \cdot [\nabla_{\parallel} \cdot \langle \hat{I}_{q1}^{(4)} \mathbf{v}_{1\parallel}^{\delta 0}, \mathbf{v}_{1\parallel}^{d0} \rangle] + \langle \hat{I}_{q1}^{(2)} v_{1\zeta}^{\delta 0}, v_{1\zeta}^{d0} \rangle \\ &\quad + \nabla_{\parallel} \cdot [\langle \hat{I}_{q1}^{(3)} \mathbf{v}_{1\parallel}^{\delta 0}, v_{1\zeta}^{d0} \rangle + \langle \hat{I}_{q1}^{(3)} v_{1\zeta}^{\delta 0}, \mathbf{v}_{1\parallel}^{d0} \rangle] \\ &\quad + \nabla_{\parallel} \cdot [\nabla_{\parallel} \cdot \langle \hat{I}_{q\zeta}^{(4)} \mathbf{v}_{1\parallel}^{\delta 0}, \partial_\zeta \mathbf{v}_{1\parallel}^{d0} \rangle] + \langle \hat{I}_{q\zeta}^{(2)} v_{1\zeta}^{\delta 0}, \partial_\zeta v_{1\zeta}^{d0} \rangle \\ &\quad \left. + \nabla_{\parallel} \cdot [\langle \hat{I}_{q\zeta}^{(3)} \mathbf{v}_{1\parallel}^{\delta 0}, \partial_\zeta v_{1\zeta}^{d0} \rangle + \langle \hat{I}_{q\zeta}^{(3)} v_{1\zeta}^{\delta 0}, \partial_\zeta \mathbf{v}_{1\parallel}^{d0} \rangle] \right\}, \end{aligned}$$

$$\mathbf{v}_{2\parallel}^{\delta v0} = \frac{2}{\omega \delta^2} \left\{ \nabla_{\parallel} \cdot \langle \hat{I}_{qq}^{(2)} \mathbf{v}_{1\parallel}^{\delta 0}, \mathbf{v}_{1\parallel}^{\delta 0} \rangle + \langle \hat{I}_{qq}^{(1)} \mathbf{v}_{1\parallel}^{\delta 0}, v_{1\zeta}^{\delta 0} \rangle \quad (\text{B12c}) \right.$$

$$\begin{aligned} &\quad + \nabla_{\parallel} \cdot \langle \hat{I}_{1q}^{(2)} \mathbf{v}_{1\parallel}^{d0}, \mathbf{v}_{1\parallel}^{\delta 0} \rangle + \langle \hat{I}_{1q}^{(1)} \mathbf{v}_{1\parallel}^{d0}, v_{1\zeta}^{\delta 0} \rangle \\ &\quad + \nabla_{\parallel} \cdot \langle \hat{I}_{\zeta q}^{(2)} \partial_\zeta \mathbf{v}_{1\parallel}^{d0}, \mathbf{v}_{1\parallel}^{\delta 0} \rangle + \langle \hat{I}_{\zeta q}^{(1)} \partial_\zeta \mathbf{v}_{1\parallel}^{d0}, v_{1\zeta}^{\delta 0} \rangle \\ &\quad + \nabla_{\parallel} \cdot \langle \hat{I}_{q1}^{(2)} \mathbf{v}_{1\parallel}^{\delta 0}, \mathbf{v}_{1\parallel}^{d0} \rangle + \langle \hat{I}_{q1}^{(1)} \mathbf{v}_{1\parallel}^{\delta 0}, v_{1\zeta}^{d0} \rangle \\ &\quad \left. + \nabla_{\parallel} \cdot \langle \hat{I}_{q\zeta}^{(2)} \mathbf{v}_{1\parallel}^{\delta 0}, \partial_\zeta \mathbf{v}_{1\parallel}^{d0} \rangle + \langle \hat{I}_{q\zeta}^{(1)} \mathbf{v}_{1\parallel}^{\delta 0}, \partial_\zeta v_{1\zeta}^{d0} \rangle \right\}, \end{aligned}$$

$$\mathbf{v}_{2\parallel}^{\delta 0} = \frac{2}{\omega \delta^2} \left\{ -\nabla_{\parallel} \left[\langle \hat{I}_{qq}^{(2)} v_{1\zeta}^{\delta 0}, v_{1\zeta}^{\delta 0} \rangle \quad (\text{B12d}) \right.$$

$$\begin{aligned} &\quad + \langle \hat{I}_{1q}^{(2)} v_{1\zeta}^{d0}, v_{1\zeta}^{\delta 0} \rangle + \langle \hat{I}_{q1}^{(2)} v_{1\zeta}^{\delta 0}, v_{1\zeta}^{d0} \rangle \\ &\quad + \nabla_{\parallel} \cdot \langle \hat{I}_{qq}^{(2)} \mathbf{v}_{1\parallel}^{\delta 0}, \mathbf{v}_{1\parallel}^{\delta 0} \rangle + \langle \hat{I}_{qq}^{(1)} \mathbf{v}_{1\parallel}^{\delta 0}, v_{1\zeta}^{\delta 0} \rangle \\ &\quad + \nabla_{\parallel} \cdot \langle \hat{I}_{1q}^{(2)} \mathbf{v}_{1\parallel}^{d0}, \mathbf{v}_{1\parallel}^{\delta 0} \rangle + \langle \hat{I}_{1q}^{(1)} \mathbf{v}_{1\parallel}^{d0}, v_{1\zeta}^{\delta 0} \rangle \\ &\quad + \nabla_{\parallel} \cdot \langle \hat{I}_{\zeta q}^{(2)} \mathbf{v}_{1\parallel}^{\delta 0}, \mathbf{v}_{1\parallel}^{d0} \rangle + \langle \hat{I}_{\zeta q}^{(1)} \mathbf{v}_{1\parallel}^{\delta 0}, v_{1\zeta}^{d0} \rangle \\ &\quad + \nabla_{\parallel} \cdot \langle \hat{I}_{q1}^{(2)} \mathbf{v}_{1\parallel}^{\delta 0}, \mathbf{v}_{1\parallel}^{d0} \rangle + \langle \hat{I}_{q1}^{(1)} \mathbf{v}_{1\parallel}^{\delta 0}, v_{1\zeta}^{d0} \rangle \\ &\quad \left. + \langle \hat{I}_{q\zeta}^{(1)} \partial_\zeta \mathbf{v}_{1\parallel}^{d0}, v_{1\zeta}^{\delta 0} \rangle + \langle \hat{I}_{q\zeta}^{(1)} \mathbf{v}_{1\parallel}^{\delta 0}, \partial_\zeta v_{1\zeta}^{d0} \rangle \right\}, \end{aligned}$$

$$\begin{aligned}
v_{2\zeta}^{\delta 0} = v_{2\zeta}^{\delta p 0} + v_{2\zeta}^{\delta v 0} = & -\frac{2}{\omega\delta^2} \left\{ \right. \\
& + \nabla_{\parallel} \cdot \left[\nabla_{\parallel} \cdot \langle \hat{I}_{qq}^{(3)} \mathbf{v}_{1\parallel}^{\delta 0}, \mathbf{v}_{1\parallel}^{\delta 0} \rangle + \langle \hat{I}_{qq}^{(2)} \mathbf{v}_{1\parallel}^{\delta 0}, v_{1\zeta}^{\delta 0} \rangle \right] \\
& + \nabla_{\parallel} \cdot \left[\nabla_{\parallel} \cdot \langle \hat{I}_{1q}^{(3)} \mathbf{v}_{1\parallel}^{\delta 0}, \mathbf{v}_{1\parallel}^{\delta 0} \rangle + \langle \hat{I}_{1q}^{(2)} \mathbf{v}_{1\parallel}^{\delta 0}, v_{1\zeta}^{\delta 0} \rangle \right] \\
& + \nabla_{\parallel} \cdot \left[\nabla_{\parallel} \cdot \langle \hat{I}_{\zeta q}^{(3)} \partial_{\zeta} \mathbf{v}_{1\parallel}^{\delta 0}, \mathbf{v}_{1\parallel}^{\delta 0} \rangle + \langle \hat{I}_{\zeta q}^{(2)} \partial_{\zeta} \mathbf{v}_{1\parallel}^{\delta 0}, v_{1\zeta}^{\delta 0} \rangle \right] \\
& + \nabla_{\parallel} \cdot \left[\nabla_{\parallel} \cdot \langle \hat{I}_{q1}^{(3)} \mathbf{v}_{1\parallel}^{\delta 0}, \mathbf{v}_{1\parallel}^{\delta 0} \rangle + \langle \hat{I}_{q1}^{(2)} \mathbf{v}_{1\parallel}^{\delta 0}, v_{1\zeta}^{\delta 0} \rangle \right] \\
& \left. + \nabla_{\parallel} \cdot \left[\nabla_{\parallel} \cdot \langle \hat{I}_{q\zeta}^{(3)} \mathbf{v}_{1\parallel}^{\delta 0}, \partial_{\zeta} \mathbf{v}_{1\parallel}^{\delta 0} \rangle + \langle \hat{I}_{q\zeta}^{(2)} \mathbf{v}_{1\parallel}^{\delta 0}, \partial_{\zeta} v_{1\zeta}^{\delta 0} \rangle \right] \right\}. \tag{B12e}
\end{aligned}$$

Appendix C: Implementation in COSMOL of the 2nd-order boundary condition

The basic COMSOL Multiphysics syntax for implementing the BL25 model is presented in Sec. VI together with the COMSOL implementation (written in the “tt-typeface”) of the BL25 fluid-solid first-order boundary conditions. To implement the more involved 2nd-order BL25 slip-velocity boundary condition Eq. (39), we need to provide COMSOL implementations for terms of the form (A) $\nabla_{\parallel} \langle \hat{I}_{qq}^{(2)} v_{1\zeta}^{\delta 0}, v_{1\zeta}^{\delta 0} \rangle$, (B) $\nabla_{\parallel} \cdot \langle \hat{I}_{qq}^{(2)} \mathbf{v}_{1\parallel}^{\delta 0}, \mathbf{v}_{1\parallel}^{\delta 0} \rangle$, and (C) $\langle \hat{I}_{q\zeta}^{(1)} \mathbf{v}_{1\parallel}^{\delta 0}, \partial_{\zeta} v_{1\zeta}^{\delta 0} \rangle$ from Eq. (35b); (D) $\nabla_{\parallel} \cdot \nabla_{\parallel} \cdot \langle \hat{I}_{qq}^{(3)} \mathbf{v}_{1\parallel}^{\delta 0}, \mathbf{v}_{1\parallel}^{\delta 0} \rangle$ and (E) $\nabla_{\parallel} \cdot \langle \hat{I}_{q1}^{(2)} \mathbf{v}_{1\parallel}^{\delta 0}, v_{1\zeta}^{\delta 0} \rangle$ from Eq. (35c); and (F) $\langle \mathbf{iV}_1^0 \cdot \nabla \mathbf{v}_1^{d0} + \nabla_{\parallel} \mathbf{v}_1^{\delta 0} \rangle + \langle V_{1\zeta}^0, k_s \mathbf{v}_1^{\delta 0} \rangle$ from Eq. (38). In the following, we implement (A)-(F) term by term. However, we note that in expressions containing a parallel vector $\mathbf{v}_{1\parallel}^{\delta 0}$, it is easier to implement the full vector $\mathbf{v}_1^{\delta 0}$, and then project the final result onto the tangential plane spanned by the tangent vector \mathbf{t}_1 and \mathbf{t}_2 . The procedure is exemplified as follows:

$$\nabla_{\parallel} \cdot \langle \hat{I}_{qq}^{(2)} \mathbf{v}_{1\parallel}^{\delta 0}, \mathbf{v}_{1\parallel}^{\delta 0} \rangle = (\mathbf{W} \cdot \mathbf{t}_1) \mathbf{t}_1 + (\mathbf{W} \cdot \mathbf{t}_2) \mathbf{t}_2, \tag{C1a}$$

$$\text{for } \mathbf{W} = \nabla_{\parallel} \cdot \langle \hat{I}_{qq}^{(2)} \mathbf{v}_1^{\delta 0}, \mathbf{v}_1^{\delta 0} \rangle. \tag{C1b}$$

In each term, the tangential derivative ∇_{\parallel} projects one of the velocity fields onto the tangential plane, but not the other. Hence the necessity of the final tangent-plane projection. In COMSOL, the K th component of the tangent-plane projection of \mathbf{W} is given by the expression “(WX*t1X+WY*t1Y+WZ*t1Z)*t1K + (WX*t2X+WY*t2Y+WZ*t2Z)*t2K”.

(A) Introducing the tangential divergence “divparvd10 = vd1XtX+vd1YtY+vd1ZtZ”, $v_{1\zeta}^{\delta 0}$ is given by Eq. (20) as “vd1zeta = (i/ks)*divparvd10”. Next, with “twoOVERomgdsqr” being the pre-factor $\frac{2}{\omega\delta^2}$, all factors $\hat{I}_{ab}^{(n)}$ of Eq. (33) multiplied by $\frac{2}{\omega\delta^2}$ are called “Jabn”, e.g., “Jqz2 = twoOVERomgdsqr*(-(1-i)/2)*dvisc^3”. With “Jqq2vd1zetavd1zeta = 1/2*realdot(Jqq2*vd1zeta,vd1zeta)”, the k th component of the tangential gradient $\frac{2}{\omega\delta^2} \nabla_{\parallel} \langle \hat{I}_{qq}^{(2)} v_{1\zeta}^{\delta 0}, v_{1\zeta}^{\delta 0} \rangle$ is implemented as “dtang(Jqq2vd1zetavd1zeta,k)” followed by the tangent-plane projection (C1).

$$(B) \text{ Since } \nabla_{\parallel} \cdot \langle \hat{I}_{qq}^{(2)} \mathbf{v}_{1\parallel}^{\delta 0}, \mathbf{v}_{1\parallel}^{\delta 0} \rangle = \langle \hat{I}_{qq}^{(2)} \mathbf{v}_{1\parallel}^{\delta 0}, \nabla_{\parallel} \cdot$$

$\mathbf{v}_{1\parallel}^{\delta 0} \rangle + \langle \hat{I}_{qq}^{(2)} \nabla_{\parallel} \mathbf{v}_{1\parallel}^{\delta 0}, \mathbf{v}_{1\parallel}^{\delta 0} \rangle$, we introduce for $K = X, Y$, and Z the intermediate variable “Jqq2vd1KDIVvd10 = 0.5*realdot(Jqq2*vd1K,divparvd10)” together with “Jqq2DOTGRADvd1Kvd10 = 0.5*realdot(Jqq2*vd1KtX, vd1X) + 0.5*realdot(Jqq2*vd1KtY, vd1Y)” + 0.5*realdot(Jqq2*vd1KtZ, vd1Z)”. Consequently, the K th component of $\frac{2}{\omega\delta^2} \nabla_{\parallel} \cdot \langle \hat{I}_{qq}^{(2)} \mathbf{v}_{1\parallel}^{\delta 0}, \mathbf{v}_{1\parallel}^{\delta 0} \rangle$ is implemented as “Jqq2vd1KDIVvd10 + Jqq2DOTGRADvd1Kvd10” followed by the tangent-plane projection (C1).

(C) Using Eq. (15a) and the tangential divergence, we find $\partial_{\zeta} v_{1\zeta}^{d0} = \nabla \cdot \mathbf{v}_1^{d0} - \nabla_{\parallel} \cdot \mathbf{v}_1^{d0} = i\omega\kappa_0 p_1^0 - \nabla_{\parallel} \cdot \mathbf{v}_1^{d0}$, and therefore we introduce the variables “divparvf10 = vf1XtX+vf1YtY+vf1ZtZ” and “vf1zetazeta = i*kap0*omega*p1-divparvf10”. The K th component of $\frac{2}{\omega\delta^2} \langle \hat{I}_{q\zeta}^{(1)} \mathbf{v}_{1\parallel}^{\delta 0}, \partial_{\zeta} v_{1\zeta}^{d0} \rangle$ is then simply implemented as 0.5*realdot(Jqz1*vd1K,vf1zetazeta)”, followed by the tangent-plane projection (C1).

(D) $\nabla_{\parallel} \cdot \nabla_{\parallel} \cdot \langle \hat{I}_{qq}^{(3)} \mathbf{v}_{1\parallel}^{\delta 0}, \mathbf{v}_{1\parallel}^{\delta 0} \rangle = \nabla_{\parallel} \cdot \nabla_{\parallel} \cdot \langle \hat{I}_{qq}^{(3)} \mathbf{v}_1^{\delta 0}, \mathbf{v}_1^{\delta 0} \rangle$, since the two tangential divergences ensure that the full 3D vectors are projected onto the tangent plane. Now, the K th component of the vector resulting after the first ∇_{\parallel} is “DIVJqq3vd1Kvd1 = 0.5*(dtang(realdot(Jqq3*vd1K,vd1X),x) + dtang(realdot(Jqq3*vd1K,vd1Y),y) + dtang(realdot(Jqq3*vd1K,vd1Z),z))”. So $\frac{2}{\omega\delta^2} \nabla_{\parallel} \cdot \nabla_{\parallel} \cdot \langle \hat{I}_{qq}^{(3)} \mathbf{v}_{1\parallel}^{\delta 0}, \mathbf{v}_{1\parallel}^{\delta 0} \rangle$ is simply implemented as “dtang(DIVJqq3vd1Xvd1,x)+dtang(DIVJqq3vd1Yvd1,y)+dtang(DIVJqq3vd1Zvd1,z)”.

(E) $\nabla_{\parallel} \cdot \langle \hat{I}_{q1}^{(2)} \mathbf{v}_{1\parallel}^{\delta 0}, v_{1\zeta}^{d0} \rangle = \nabla_{\parallel} \cdot \langle \hat{I}_{q1}^{(2)} \mathbf{v}_1^{\delta 0}, v_{1\zeta}^{d0} \rangle$, since the tangential divergence ensures that $\mathbf{v}_1^{\delta 0}$ is projected onto the tangent plane. The K th component of the argument to the divergence is implemented as “Jq12vd1Kvf1zeta = 0.5*realdot(Jq12*vd1X,vf1zeta)”, and therefore, $\frac{2}{\omega\delta^2} \nabla_{\parallel} \cdot \langle \hat{I}_{q1}^{(2)} \mathbf{v}_{1\parallel}^{\delta 0}, v_{1\zeta}^{d0} \rangle$ is implemented simply as “dtang(Jq12vd1Xvf1zeta,x) + dtang(Jq12vd1Yvf1zeta,y) + dtang(Jq12vd1Zvf1zeta,z)”.

(F) The Stokes drift contribution is the term $\frac{1}{\omega} [\langle \mathbf{iV}_1^0 \cdot \nabla \mathbf{v}_1^{d0} + \nabla_{\parallel} \mathbf{v}_1^{\delta 0} \rangle + \langle V_{1\zeta}^0, k_s \mathbf{v}_1^{\delta 0} \rangle]$. Its K th component is implemented as “vSD2K = 0.5/omega*(realdot(i*vs1X,vf1KX+vd1XtX) + realdot(i*vs1Y, vf1KY+vd1XtY) + realdot(i*vs1Z, vf1KZ+vd1XtZ) + realdot(vs1zeta,ks*vd1K))”. The perpendicular component is given by “vSD2zeta = nX*vSD2X + nY*vSD2Y + nZ*vSD2Z” and the K th component of the tangential projection is “vSD2parK = vSD2K-nK*vSD2zeta”.

The final BL25-model slip-velocity boundary condition (39) is obtained by adding all terms of the six basic forms (A)-(F). One form may have several contributions with different pre-factors “Jabn”, $a, b = 1, q, \zeta$ and $n = 1, 2, 3$, and different velocity components.

Appendix D: Mesh convergence study

We have performed a standard mesh-convergence study [22]. In 2D simulations, the solid PMMA, glue

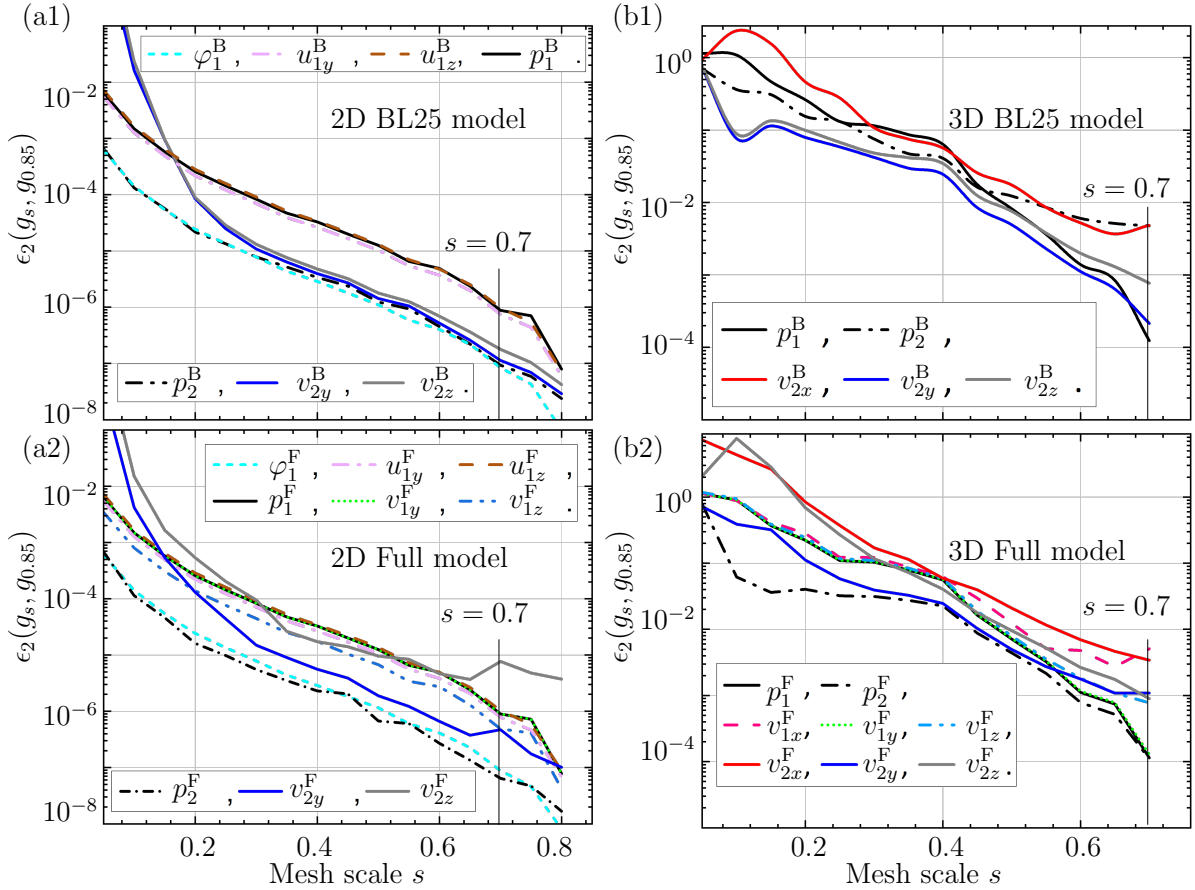


FIG. 5. Semilog mesh-convergence plot of the relative deviation $\epsilon_2(g_s, g_{0.85})$ defined in Eq. (43) versus the scaling parameter s . (a1) BL25 model in 2D: field components in 1st order φ_1^B , u_{1y}^B , u_{1z}^B , and p_1^B , and in 2nd order p_2^B , v_{2y}^B , and v_{2z}^B . (a2) Full model in 2D: field components in 1st order φ_1^F , u_{1y}^F , u_{1z}^F , p_1^F , v_{1y}^F , and v_{1z}^F , and in 2nd order p_2^F , v_{2y}^F , and v_{2z}^F . (b1) BL25 model in 3D: field components in 1st order p_1^B , and in 2nd order p_2^B , v_{2x}^B , v_{2y}^B , and v_{2z}^B . (b2) Full model in 3D: field components in 1st order p_1^F , v_{1x}^F , v_{1y}^F , and in 2nd order v_{1z}^F , p_2^F , v_{2x}^F , v_{2y}^F and v_{2z}^F .

layer, and PZT domains are discretized using a free triangular mesh with maximum and minimum element size $h_{\max}^{\text{sl}} = 0.4H_f/s$ and $h_{\min}^{\text{sl}} = 0.025h_{\max}^{\text{sl}}$, where s is the scaling parameter that is gradually increased for refining the mesh. Since the electrode thickness is small, we have used the COMSOL mapped mesh with 40 as the number of elements for smoothing the mesh from the glue layer to the PZT. For the fluid domain, we defined maximum and minimum element size as $h_{\max}^{\text{fl}} = h_{\min}^{\text{sl}}$ and $h_{\min}^{\text{fl}} = 0.12h_{\max}^{\text{fl}}$. Further, we have used the boundary layer mesh to accurately capture velocity fields in the Full model. The boundary-layer field is defined across the fluid-solid interface using 8 layers, with the first layer of 0.2δ and a stretching factor of 1.2 so that we have in total depth of 3.4δ .

In the case of the Full model in 3D, the solid PMMA domain is discretized using the free triangular mesh with maximum and minimum element size $h_{\max}^{\text{sl}} = 0.7H_f/s$ and $h_{\min}^{\text{sl}} = 0.125h_{\max}^{\text{sl}}$. Since the thin-film transducer is of thickness of $2\ \mu\text{m}$, we discretized the transducer using the structured swept mesh with the swept directed

from the top surface of the thin-film transducer. We discretized the fluid domain with a triangular mesh of maximum and minimum element size $h_{\max}^{\text{fl}} = h_{\min}^{\text{sl}}$ and $h_{\min}^{\text{fl}} = 0.6h_{\max}^{\text{fl}}$. Since a much finer mesh is required at the fluid-solid interface for the Full model to converge, we have used an edge mesh at the interface with maximum element size $h_{\max}^{\text{edge}} = 0.45h_{\max}^{\text{fl}}$. Further, we have implemented the boundary-layer mesh using 8 layers to resolve the boundary-layer fields with the first-layer thickness set to 0.2δ .

For the BL25 model in 3D, we use a much coarser mesh inside the fluid domain and we do not need a boundary-layer mesh. Accordingly, the solid PMMA domain is discretized using the triangular mesh with maximum and minimum element size $h_{\max}^{\text{sl}} = 0.4H_f/s$ and $h_{\min}^{\text{sl}} = 0.2h_{\max}^{\text{sl}}$. Similar to the 3D Full model, we use a swept mesh for the thin-film transducer, and coarser triangular mesh in the fluid domain with maximum and minimum element size $h_{\max}^{\text{fl}} = h_{\min}^{\text{sl}}$ and $h_{\min}^{\text{fl}} = 0.6h_{\max}^{\text{fl}}$. In Fig. 5, the relative deviation $\epsilon_2(g_s, g_{0.85})$, defined in Eq. (43), of the solution g_s with mesh scale s from the

solution $g_{0.85}$ with the maximum mesh scale $s = 0.85$ (the

finest mesh), is plotted in a semilog plot versus the mesh scale s for both the 2D and the 3D simulation model.

-
- [1] T. Laurell and A. Lenshof, eds., *Microscale Acoustofluidics* (Royal Society of Chemistry, Cambridge, 2015).
- [2] Y. Fan, X. Wang, J. Ren, F. Lin, and J. Wu, Recent advances in acoustofluidic separation technology in biology, *Microsyst. Nanoeng.* **8**, 94 (2022).
- [3] D. Van Assche, E. Reithuber, W. Qiu, T. Laurell, B. Henriques-Normark, P. Mellroth, P. Ohlsson, and P. Augustsson, Gradient acoustic focusing of sub-micron particles for separation of bacteria from blood lysate, *Sci. Rep.* **10**, 3670 (2020).
- [4] E. U. Anand, C. Magnusson, A. Lenshof, Y. Ceder, H. Lilja, and T. Laurell, Two-step acoustophoresis separation of live tumor cells from whole blood, *Anal. Chem.* **93**, 17076 (2021).
- [5] M. Anwar, N. M. Reis, C. Zhang, A. Khan, K. A. Kalhor, A. U. Rehman, Y. Zhang, and Z. Liu, Microfluidic devices for the isolation and label-free identification of circulating tumor cells, *J. Chem. Eng.* **499**, 156497 (2024).
- [6] W. Qiu, T. Baasch, and T. Laurell, Enhancement of acoustic energy density in bulk-wave-acoustophoresis devices using side actuation, *Phys. Rev. Applied* **17**, 044043 (2022).
- [7] T. Baasch, W. Qiu, and T. Laurell, Whole-channel acoustic energy and acoustophoretic efficiency frequency spectrum by the in-flow focusing method, *Phys. Rev. Applied* **22**, 044049 (2024).
- [8] M. Wu, A. Ozelcik, J. Rufo, Z. Wang, R. Fang, and T. J. Huang, Acoustofluidic separation of cells and particles, *Microsyst. Nanoeng.* **5**, 32 (2019).
- [9] E. Hemachandran, S. Z. Hoque, T. Laurell, and A. K. Sen, Reversible stream drop transition in a microfluidic coflow system via on demand exposure to acoustic standing waves, *Phys. Rev. Lett.* **127**, 134501 (2021).
- [10] S. Z. Hoque and A. K. Sen, Dynamics of a two-layer immiscible fluid system exposed to ultrasound, *The Journal of the Acoustical Society of America* **155**, 1655 (2024).
- [11] S. Deshmukh, Z. Brzozka, T. Laurell, and P. Augustsson, Acoustic radiation forces at liquid interfaces impact the performance of acoustophoresis, *Lab Chip* **14**, 3394 (2014).
- [12] J. T. Karlsen, P. Augustsson, and H. Bruus, Acoustic force density acting on inhomogeneous fluids in acoustic fields, *Phys. Rev. Lett.* **117**, 114504 (2016).
- [13] P. Augustsson, J. T. Karlsen, H.-W. Su, H. Bruus, and J. Voldman, Iso-acoustic focusing of cells for size-insensitive acousto-mechanical phenotyping, *Nat. Commun.* **7**, 11556 (2016).
- [14] J. T. Karlsen, W. Qiu, P. Augustsson, and H. Bruus, Acoustic streaming and its suppression in inhomogeneous fluids, *Phys. Rev. Lett.* **120**, 054501 (2018).
- [15] A. Lenshof, M. Evander, T. Laurell, and J. Nilsson, Acoustofluidics 5: Building microfluidic acoustic resonators, *Lab Chip* **12**, 684 (2012).
- [16] W. J. Savage, J. R. Burns, and J. Fiering, Safety of acoustic separation in plastic devices for extracorporeal blood processing, *Transfusion* **57**, 1818 (2017).
- [17] C. Yang, Z. Li, P. Li, W. Shao, P. Bai, and Y. Cui, Acoustic particle sorting by integrated micromachined ultrasound transducers on polymerbased microchips, *IEEE International Ultrasonics Symposium (IUS)*, 1 (2017).
- [18] R. Silva, P. Dow, R. Dubay, C. Lissandrello, J. Holder, D. Densmore, and J. Fiering, Rapid prototyping and parametric optimization of plastic acoustofluidic devices for blood-bacteria separation, *Biomedical Microdevices* **19**, 70 (2017).
- [19] R. Dubay, C. Lissandrello, P. Swierk, N. Moore, D. Doty, and J. Fiering, Scalable high-throughput acoustophoresis in arrayed plastic microchannels, *Biomicrofluidics* **13**, 034105 (2019).
- [20] F. Lickert, M. Ohlin, H. Bruus, and P. Ohlsson, Acoustophoresis in polymer-based microfluidic devices: Modeling and experimental validation, *J. Acoust. Soc. Am.* **149**, 4281 (2021).
- [21] R. P. Moiseyenko and H. Bruus, Whole-system ultrasound resonances as the basis for acoustophoresis in all-polymer microfluidic devices, *Phys. Rev. Applied* **11**, 014014 (2019).
- [22] P. B. Muller, R. Barnkob, M. J. H. Jensen, and H. Bruus, A numerical study of microparticle acoustophoresis driven by acoustic radiation forces and streaming-induced drag forces, *Lab Chip* **12**, 4617 (2012).
- [23] P. B. Muller, M. Rossi, A. G. Marin, R. Barnkob, P. Augustsson, T. Laurell, C. J. Kähler, and H. Bruus, Ultrasound-induced acoustophoretic motion of microparticles in three dimensions, *Phys. Rev. E* **88**, 023006 (2013).
- [24] P. B. Muller and H. Bruus, Numerical study of thermoviscous effects in ultrasound-induced acoustic streaming in microchannels, *Phys. Rev. E* **90**, 043016 (2014).
- [25] P. Hahn and J. Dual, A numerically efficient damping model for acoustic resonances in microfluidic cavities, *Physics of Fluids* **27**, 062005 (2015).
- [26] M. W. H. Ley and H. Bruus, Continuum modeling of hydrodynamic particle-particle interactions in microfluidic high-concentration suspensions, *Lab on a Chip* **16**, 1178 (2016).
- [27] B. Hammarström, T. Laurell, and J. Nilsson, Seed particle enabled acoustic trapping of bacteria and nanoparticles in continuous flow systems, *Lab Chip* **12**, 4296 (2012).
- [28] M. Antfolk, C. Magnusson, P. Augustsson, H. Lilja, and T. Laurell, Acoustofluidic, label-free separation and simultaneous concentration of rare tumor cells from white blood cells, *Anal. Chem.* **87**, 9322 (2015).
- [29] Z. Mao, P. Li, M. Wu, H. Bachman, N. Mesyngier, X. Guo, S. Liu, F. Costanzo, and T. J. Huang, Enriching nanoparticles via acoustofluidics, *ACS Nano* **11**, 603 (2017).
- [30] D. J. Collins, Z. Ma, J. Han, and Y. Ai, Continuous micro-vortex-based nanoparticle manipulation via focused surface acoustic waves, *Lab Chip* **17**, 91 (2017).
- [31] J. S. Bach and H. Bruus, Theory of pressure acoustics with viscous boundary layers and streaming in curved

- elastic cavities, *J. Acoust. Soc. Am.* **144**, 766 (2018).
- [32] W. L. Nyborg, Acoustic streaming near a boundary, *J. Acoust. Soc. Am.* **30**, 329 (1958).
- [33] C. Lee and T. Wang, Near-boundary streaming around a small sphere due to 2 orthogonal standing waves, *J. Acoust. Soc. Am.* **85**, 1081 (1989).
- [34] J. Vanneste and O. Bühler, Streaming by leaky surface acoustic waves, *Proc. R. Soc. A* **467**, 1779 (2011).
- [35] N. R. Skov, J. S. Bach, B. G. Winckelmann, and H. Bruus, 3D modeling of acoustofluidics in a liquid-filled cavity including streaming, viscous boundary layers, surrounding solids, and a piezoelectric transducer, *AIMS Mathematics* **4**, 99 (2019).
- [36] S. M. Hagsäter, T. G. Jensen, H. Bruus, and J. P. Kutter, Acoustic resonances in microfluidic chips: full-image micro-PIV experiments and numerical simulations, *Lab Chip* **7**, 1336 (2007).
- [37] See Supplemental Material at <https://bruus-lab.dk/Hoque-BL25-Suppl.pdf> for an analysis of corner effects in rectangular channels and for details on the dependency on the glue-layer thickness.
- [38] *Glass Silicon Constraint Substrates*, CORNING, Houghton Park C-8, Corning, NY 14831, USA, <http://www.valleydesign.com/Datasheets/Corning%20Pyrex%207740.pdf>, accessed 7 July 2025.
- [39] W. N. Bodé, F. Lickert, P. Augustsson, and H. Bruus, Determination of the complex-valued elastic moduli of polymers by electrical-impedance spectroscopy for ultrasound applications, *Phys. Rev. Appl.* **18**, 064078 (2022).
- [40] A. G. Steckel, H. Bruus, P. Muralt, and R. Matloub, Fabrication, characterization, and simulation of glass devices with AlN thin-film transducers for excitation of ultrasound resonances, *Phys. Rev. Applied* **16**, 014014, 1 (2021).
- [41] A. G. Steckel and H. Bruus, Numerical study of bulk acoustofluidic devices driven by thin-film transducers and whole-system resonance modes, *J. Acoust. Soc. Am.* **150**, 634 (2021).
- [42] *COMSOL Multiphysics 6.2*, COMSOL (2023), <http://www.comsol.com>.
- [43] J. H. Joergensen and H. Bruus, Theory and modeling of nonperturbative effects in thermoviscous acoustofluidics, *Phys. Rev. E* **107**, 015106 (2023).
- [44] M. Antfolk, P. B. Müller, P. Augustsson, H. Bruus, and T. Laurell, Focusing of sub-micrometer particles and bacteria enabled by two-dimensional acoustophoresis, *Lab Chip* **14**, 2791 (2014).
- [45] N.-S. Cheng, Formula for the viscosity of a glycerol-water mixture, *Ind. Eng. Chem. Res.* **47**, 3285 (2008).
- [46] W. N. Bodé, L. Jiang, T. Laurell, and H. Bruus, Microparticle acoustophoresis in aluminum-based acoustofluidic devices with PDMS covers, *Micromachines* **11**, 292 (2020).
- [47] M. A. Caro, S. Zhang, T. Riekkinen, M. Ylilammi, M. A. Moram, O. Lopez-Acevedo, J. Molarius, and T. Laurila, Piezoelectric coefficients and spontaneous polarization of ScAlN, *J. Phys.-Condens. Mat.* **27**, 245901 (2015).
- [48] R. H. Olsson, Z. Tang, and M. D'Agati, Doping of aluminum nitride and the impact on thin film piezoelectric and ferroelectric device performance, in *2020 IEEE Custom Integrated Circuits Conference (CICC)* (2020) pp. 1–6.
- [49] *Pz27 soft PZT*, CTS|Ferroperm, Porthusvej 4, DK-3490 Kvistgaard, Denmark (2025), <https://www.ctscorp.com/Product-Series/Pz27.htm>, accessed 7 July 2025.
- [50] *Pz26 hard PZT*, CTS|Ferroperm, Porthusvej 4, DK-3490 Kvistgaard, Denmark (2025), <https://www.ctscorp.com/Product-Series/Pz26.htm>, accessed 7 July 2025.